ACS APPLIED MATERIALS & INTERFACES

Research Article

www.acsami.org

Rapid Aluminum Nanoparticle Production by Milling in NH_3 and CH_3NH_2 Atmospheres: An Experimental and Theoretical Study

Brandon W. McMahon,[†] Jiang Yu,[†] Jerry A. Boatz,[‡] and Scott L. Anderson*,[†]

[†]Department of Chemistry, University of Utah, 315 S. 1400 E., Salt Lake City, Utah 84112, United States

[‡]Propellants Branch, Rocket Propulsion Division, Aerospace Systems Directorate, Air Force Research Laboratory, AFMC AFRL/RQRP, 10 East Saturn Boulevard, Edwards AFB, California 93524, United States

Supporting Information

ABSTRACT: Ball milling of aluminum in gaseous atmospheres of ammonia and monomethylamine (MMA) was found to produce particles in the 100 nm size range with high efficiency. A combination of mass spectrometry, X-ray photoelectron spectroscopy (XPS), thermogravimetric analysis with mass spectrometric product analysis (TGA-MS), scanning electron microscopy (SEM), infrared spectroscopy, and dynamic light scattering (DLS) was used to study the particles and the chemical interactions responsible for particle production. To help understand the nature of the surface chemistry, high level quantum chemical calculations were performed to predict the structures and energetics for binding and reactions of NH_3 and MMA on aluminum surfaces. Both NH_3 and MMA react with aluminum under milling conditions, producing H_2 and other gaseous products, and leaving the surfaces functionalized. The surface functionalization enhances size reduction by reducing the surface free energy and the tendency toward mechanochemical welding. For both NH_3 and MMA, the particle cores are metallic aluminum, but the surface chemical properties are quite different. The ammonia-milled particles are capped by an $AlN_xO_yH_z$ layer ~10 nm thick, which passivates the particles. The MMA-milled particles are capped with a thinner passivating layer, such that they are pyrophoric in air and react with N_2 at elevated temperatures.

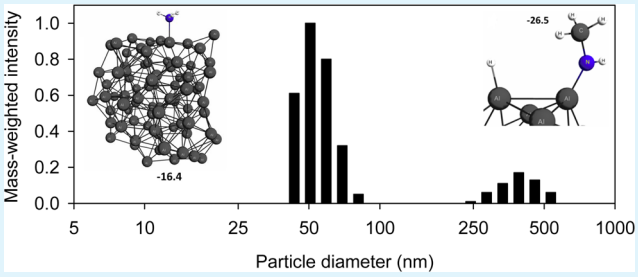

KEYWORDS: *milling, nanoparticle synthesis, aluminum, ammonia, monomethylamine*

I. INTRODUCTION

Aluminum powder in the micron size range has been extensively used as a high energy density fuel and fuel additive in propulsion and pyrotechnic applications,[1−5] due to its high volumetric energy density (~81 MJ/L), more than double that of hydrocarbon fuels. Reducing the particle size reduces the ignition and combustion times,[6−12] but the presence of a native oxide layer on the particles means that the oxide becomes a significant portion of the particle mass for particle diameters less than 100 nm.[10] Therefore, methods for production of aluminum particles capped by a layer that minimizes oxide layer formation during air exposure are potentially useful, particularly if the method is inexpensive and can be scaled to generate quantities needed for practical applications. Here, we present a study of aluminum ball milling in reactive atmospheres, which efficiently generates particles in the 100 nm size range efficiently and caps them with an amine or nitride-like layer. The particles can be further functionalized after production to aid in separation, improve dispersibility in media such as hydrocarbons or other fuels, and improve stability upon air exposure. Particles produced by milling in NH_3 are found to be relatively inert; hence, they are interesting primarily from the perspective of understanding the production mechanism. Particles produced by milling in monomethylamine, however, are highly reactive, spontaneously igniting in air unless they are further passivated. Such particles should be of interest for energetics applications; however, typical methods used to measure energy content (e.g., calorimetry) are difficult to apply, because the particles ignite on exposure to oxidizers. We, therefore, focus the present report on production and characterization of the particles, including demonstration that the particles react with N_2 at temperatures above the Al melting point.

High energy ball milling typically involves milling feedstock of the material of interest, together with balls or other media of some hard, dense material, such that feedstock particles are crushed during media−media and media−wall collisions. The efficiency of size reduction depends on a number of factors.[13−17] Brittle materials tend to fracture under mechanical stress, whereas ductile/malleable materials can also undergo plastic deformation rather than cracking. Size reduction by fracturing is counteracted by mechanochemical (cold) welding, which tends to result in particle aggregation and fusion. Production of nanoscale powder results in an enormous increase in surface area; thus, one critical factor is the free energy associated with the creation of new surface area. Almost

Received: June 1, 2015
Accepted: July 1, 2015
Published: July 1, 2015

DOI: 10.1021/acsami.5b04806
ACS Appl. Mater. Interfaces 2015, 7, 16101−16116

70 years ago, Rehbinder noted that adsorption of surface-active agents lowers the surface free energy,[18] and as a result, the energy required for crack formation and propagation is lowered, embrittling the material and enhancing size reduction.[19,20] Formation of an adsorbate layer may also reduce the tendency toward particle welding.

Typically, agents used in ball milling are liquids and can be present either to simply disperse particles or to bind to and modify the properties of the particle surfaces. The use of liquid reagents to enhance reactions and improve the efficiency of mechanochemical syntheses is also a well-established practice.[21−25] We recently reported[26] a study of the effects of a variety of liquid reactants and solutions on production of nanoparticles by milling aluminum, iron, and copper under conditions where no particles are produced by milling in nonreactive liquids (e.g., hexane). For the two softer metals (Cu and Al), this approach produced mixtures of nano- and micron-sized particles, with nanoparticles making up less than 50% of the product mass under the best conditions. Although it is straightforward to separate the nano- and microparticles by sedimentation, it would clearly be better to generate only the desired nanoparticles. The mechanism for size reduction during milling in surface-active liquids is complex, because, in addition to modifying surface chemistry, the liquids can affect mechanical aspects of the process by lubricating interfaces, dissipating local heating by vaporization, and affecting transport to and from particle surfaces.

Here, we report a study of nanoparticle production by dry milling aluminum in NH_3 and monomethylamine (MMA) atmospheres, and we compare the results to analogous milling experiments in H_2, Ar, and N_2. NH_3 and MMA were chosen because amines are known to bind to and react with aluminum surfaces.[27−33] As shown below, nanoparticle production is more efficient in these gases than in reactive liquid milling agents, including alkylamines. Furthermore, the particle size distributions are narrower, without the large concentrations of micron scale particles seen for liquid agents. Particles were characterized by a combination of dynamic light scattering, electron microscopy, infrared spectroscopy, and X-ray photoelectron spectroscopy. In addition, the chemistry during and after milling was characterized by a combination of mass spectrometry (MS) of the milling atmospheres, thermal desorption MS, and thermogravimetric analysis with MS of the evolved gases (TGA-MS). To help interpret the surface chemistry, detailed density functional theory calculations were carried out, in which atomically rough Al surfaces were modeled using an Al_{80} cluster that has a variety of surface sites and is large enough to have a core of bulk-like atoms as well.

II. EXPERIMENTAL AND THEORETICAL METHODOLOGY

A. Particle Production. Particles were produced by milling aluminum flakes in a Retsch PM 400 planetary ball mill, using Retsch 250 mL tungsten carbide jars, and ∼3 mm diameter tungsten carbide milling media. As described previously,[26] the original jar lids were replaced with 316 stainless steel lids with valved ports that can be used for evacuation, reactant introduction, and headspace sampling, via a vacuum/pressure manifold located inside an N_2-filled glovebox.

Approximately 2 g of 1 mm aluminum flakes (Sigma-Aldrich: 518573−500G) and ∼200 g of tungsten carbide milling media were added to the jar. The jar was sealed in the glovebox, evacuated, and then pumped and backfilled three times with the gas of interest to ensure that there was no significant contribution from N_2 to the nitrogen content of the products. For milling in ammonia, the jar was filled to a pressure of ∼3.7 atm (∼55 psia). Because the vapor pressure of monomethylamine (MMA) is lower, the maximum fill pressure was ∼2.2 atm (∼32 psia), with some variability from run to run due to the effects of evaporative cooling on the MMA tank pressure. To compensate for the lower initial MMA pressure, the headspace was evacuated and repressurized after each hour of milling. For both gases, the mill was operated with a sun wheel rotational frequency of 350 rpm (relative centrifugal force of ∼20 g) for 5 h.

B. Safety and Handling Considerations. NH_3 and CH_3NH_2 are highly flammable gases and severe eye and respiratory irritants. Unpassivated aluminum nanopowder is violently reactive with oxidizers such as O_2 and H_2O, and spontaneously ignites upon air exposure. Solvent-wetted particles may undergo delayed ignition. Samples were handled and stored in a N_2-filled glovebox, however, note that O_2 contamination, even at levels well below 1 ppm, is sufficient to oxidize the sample surface layer in a few seconds if reaction is efficient. Samples were, therefore, stored inside sealed vials in the glovebox, to minimize exposure to contaminants. To passivate particles under controlled conditions, we simply exposed the Al nanopowder to ∼20 milliTorr of air in the glovebox load lock chamber for a few minutes, resulting in sufficient oxidation that the particles no longer would autoignite when brought out into the laboratory.

C. Particle Analysis. Scanning electron microscopy (SEM) was done using an FEI Nova Nano 600 instrument. Samples were prepared by ultrasonicating in acetonitrile and diluting until only slightly turbid, followed by drop casting on lacey carbon transmission electron microscopy (TEM) grids. Dynamic light scattering (DLS) analyses were performed using a NICOMP 380 ZLS instrument to analyze samples dispersed in acetonitrile, and diluted until only slightly turbid. Samples prepared with NH_3 or MMA milling were somewhat prone to aggregation, and suspensions were only stable for 15 to 30 min. To minimize aggregation, the DLS samples were ultrasonicated just prior to analysis. Both SEM and DLS analysis was done on air-exposed samples.

A Kratos Axis Ultra instrument was used for X-ray photoelectron spectroscopy (XPS), using monochromatic Al Kα radiation (1486.6 eV), and 300 × 700 μm analysis area. Sample charging was compensated using a low energy electron flood gun. The samples were prepared for XPS in the glovebox, by pressing the powders directly onto carbon tape on a stainless steel sample holder. Transfers from the glovebox to the XPS instrument were made using a Kratos inert atmosphere transfer device, however, for the much more reactive MMA sample, the device was modified to allow the internal volume to be evacuated, leak-checked, and pressurized with 99.9999% argon to minimize air intrusion in case of leaks. As noted above, however, even samples handled and transferred in "inert" atmospheres inevitably receive significant exposures to oxygen-containing contaminants.

Mass spectrometry was used to analyze the headspace of the milling jars at intervals during the milling process, in order to probe reactions of NH_3 or CH_3NH_2 with aluminum under milling conditions. Headspace analysis was done on separate milling runs to minimize perturbations to the jar atmosphere, and mass spectral intensities were corrected for the variation of sensitivity with mass, based on experiments where H_2, NH_3, and N_2 were leaked into the instrument at known pressures. For gas sampling, jars were transferred into the glovebox and connected to the vacuum/pressure manifold, which was used to leak a small amount of headspace gas into a sampling vial. The sampling vial was then connected to the inlet of a quadrupole mass spectrometer, with a base pressure below 5×10^{-9} Torr. Gases were leaked into the mass spectrometer at a source pressure of $\sim 1 \times 10^{-7}$ Torr.

Thermogravimetric analysis (TGA) was used to determine the mass loss from samples during heating from 25 to 800 °C at a rate of 10 °C/min. The TA Model Q500 Thermogravimetric Analyzer is housed in an N_2-filled glovebox so that samples were not exposed to air during transfer to, or measurement in the TGA instrument. Separate experiments were done using N_2 and Ar to purge the TGA furnace and balance, to examine possible reactions with N_2. Gases evolved from the samples during TGA were analyzed by a sampling mass

DOI: 10.1021/acsami.5b04806
ACS Appl. Mater. Interfaces 2015, 7, 16101−16116

spectrometer (ThermoStar GSD301T3, Pfeiffer Vacuum), which monitored multiple mass channels as a function of time, allowing them to be correlated with the TGA temperature ramp.

Because the TGA-MS only allowed monitoring of a limited number of masses, for the MMA-milled material, we first studied the desorption mass spectrum as a function of temperature, using the same mass spectrometer used for headspace analysis. A powder sample was collected after the completion of milling, using an Ar-filled glovebox for sample collection to avoid any possibility of reaction of the aluminum nanopowder with N_2. Approximately 200 mg of powder was transferred to a glass vial which was sealed in the argon-filled glovebox, and then attached to the mass spectrometer. The gas line between the sample vial and mass spectrometer leak valve was evacuated, and then gas from the vial was leaked into the mass spectrometer at a pressure of $\sim 1 \times 10^{-7}$ Torr. An initial mass spectrum was measured, and then the sample temperature (measured by a K-type thermocouple) was increased in a series of steps, using a tube furnace, and waiting 10 min for the temperature to equilibrate before taking mass spectra. The sample vial was only opened to allow mass spectral measurements after equilibration at each temperature. As a result, the mass spectra are for gas that evolved from the powder during heating to each temperature.

Infrared spectroscopy was attempted for both the ammonia- and MMA-milled samples, using an instrument and methods previously used successfully for a variety of ligand-capped particles,[16,26,34] however, no significant absorption features were observed the NH_3- or MMA-milled aluminum particles. Diffuse reflectance and attenuated total reflection experiments were also attempted at Argonne National Lab, but again no significant spectral features were observed. The lack of signal is tentatively attributed to a combination of low reflectivity of the nanoaluminum samples, together with a relatively low concentration of IR chromaphores on the particle surfaces.

D. Density Functional Theory (DFT) calculations. To help understand the reactions of NH_3 and MMA with aluminum surfaces, DFT was used to probe the interactions between a large aluminum cluster and molecules of NH_3 or CH_3NH_2. Structures and energetics were computed using the M06 hybrid meta-generalized gradient approximation (GGA) exchange-correlation functional of Zhao and Truhlar[35] and a Lebedev quadrature grid with 99 radial and 590 angular points. The McLean-Chandler (12s,9p)/[6s,5p] contracted basis set,[36] augmented with a d-type polarization function[37] and diffuse s+p shell,[38] was used for aluminum and the 6-311++G(d,p) basis set[38,39] was used for carbon, nitrogen, and hydrogen. This combination of functional and basis sets is henceforth denoted simply as M06/6-311++G(d,p). A cluster of 80 aluminum atoms was used as a model for the surface of the aluminum particles. Its geometry was optimized from a previously reported[40] calculated geometry for an 80 atom boron cluster, and it exposes a variety of surface sites, while being large enough to have a bulk-like core. All structures reported herein were fully optimized and, unless stated otherwise, have been verified as local minima or first order transition states via diagonalization of the Hessian matrix; i.e., the mass-weighted energy second derivatives with respect to nuclear displacements. The minimum energy path, also known as the intrinsic reaction coordinate (IRC), connecting each transition state to reactants and products has been traced using the Gonzales-Schlegel second order method.[41] Relative energies include zero point vibrational energy (ZPE) corrections, obtained from the calculated harmonic vibrational frequencies which have been scaled by a factor of 0.983.[35] All calculations were performed using the GAMESS[42,43] quantum chemistry program.

The primary purpose of these computations is to determine which species may be present on the surface of aluminum particles and the reactions leading to their formation. Such reactions should be consistent, in the case of NH_3 for example, with the observed formation of H_2 during milling, and also account for the absence of other stable product molecules such as N_2, N_2H_2, and N_2H_4. The approach taken is to first consider the decomposition reactions of a single NH_3 chemisorbed on the surface of an Al_{80} cluster, followed by consideration of "bimolecular" reactions involving two neighboring chemisorbed ammonia molecules. A similar approach is applied to methylamine to determine which products may form on the nanoparticle surface from CH_3NH_2, and to identify the reactions leading to their formation. Such reactions must be consistent with the experimental observation of H_2, CH_2NH, and CH_3NHCH_3 products, as well as the absence of other stable species such as NH_3, CH_4, or CH_3CH_3.

III. RESULTS AND DISCUSSION

A. Aluminum particles from milling with NH_3. To track the progress from millimeter Al flakes to particles in the 100 nm size range, an experiment was done in which the jar was opened to allow particle sampling after each hour of milling, for a total of 5 h. The jar was refilled with NH_3 after each particle sampling operation, and this was the only NH_3 milling experiment where additional NH_3 was added during the milling process. After milling for 1 h in 3.7 atm of ammonia, the initial 2 g of aluminum flakes was reduced to a homogeneous, gray, metallic-looking powder. After a second hour of milling the material appeared homogeneously black, with no visible metallic luster, suggesting that the particle size had been reduced small enough to absorb light efficiently. Examination after 3, 4, and 5 h of milling showed no further visible changes in the milling products.

For comparison, the 1 mm Al flake starting material was also milled in neat argon (99.9999%), nitrogen, and hydrogen atmospheres at ~3 atm pressure. In all three experiments, the initial aluminum flakes were formed into 1 to 2 mm diameter particles of roughly spherical shape, with no evidence of smaller particles. Because the mass of a ~1 mm sphere is much larger than that of a ~1 mm flake, it is clear that cold welding of the aluminum flakes to form larger particles was efficient in these gases. Given that Ar certainly does not bind to aluminum, the fact that the three gases had similar effects suggests that N_2 and H_2 were also inert under milling conditions. Conversely, the fact that NH_3 milling resulted in rapid size reduction suggests that NH_3 binds to aluminum, thereby enhancing fracturing and reducing cold welding.

Another qualitative indication that NH_3 binds to, or reacts with the aluminum surfaces is the effects on subsequent reactivity of the particles with air and water. Submicron Al particles are pyrophoric in air and also react violently with liquid water unless their surfaces are passivated. Particles milled in ammonia and brought immediately out into the laboratory were not pyrophoric and did not visibly react with liquid water (i.e., no H_2 gas generation), indicating the presence of a stable passivating layer. This passivating layer was not completely inert, however, because, upon exposure to air, the particles, which were a free-flowing powder under inert atmosphere, rapidly caked and adhered strongly to the walls of the glass vial used to remove them from the glovebox. As shown below, the passivating layer contains NH_x functionality; thus, it is not surprising that the material is highly hygroscopic.

Particle sizes were analyzed using dynamic light scattering (DLS) to probe suspensions prepared by ultrasonicating a small sample of the particles in acetonitrile. The particles are not dispersible in nonpolar solvents (see Figure S5B). The particle suspensions were stable for 15−30 min, suggesting that the surfaces were functionalized such that they had at least some compatibility with the polar solvent. Figure 1 shows the bimodal mass-weighted size distribution measured for the ammonia-milled particles. The mode between 40 and 100 nm represents ~85% of the particle mass (~1.7 g), as reported by the instrument software, with the balance of the 2 g batch

DOI: 10.1021/acsami.5b04806
ACS Appl. Mater. Interfaces 2015, 7, 16101−16116

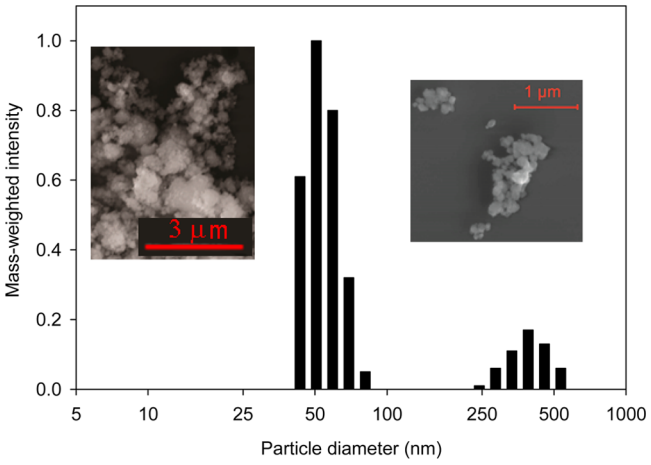

Figure 1. Dynamic light scattering measurement for ammonia milled aluminum nanoparticles in acetonitrile suspension. Insets: SEM image of the aluminum nanoparticles.

consisting of particles in the ~250−600 nm range, which could either be large particles or aggregates of smaller primary particles. SEM analysis (insets to Figure 1) showed primary particles in the size range from ~75 to ~250 nm. This is somewhat larger than the 40−100 nm size mode that dominates the DLS distribution, but the discrepancy may simply reflect the effects of particle shape, which is not taken into account in the DLS analysis. Unlike the micron size aluminum particles produced by milling in liquid milling agents, which had flattened, plate-like shapes,[26] the particles produced by NH_3-milling appear three-dimensional; however, they certainly are not spherical.

Two types of mass spectrometric analyses were used to probe reactions of NH_3 with the aluminum particles during milling and to probe the nature of volatile species present on the surfaces of the final particles. The milling jar headspace gas was analyzed prior to, and after 1 and 2 h of milling, with the results shown in Figure 2. The mass spectrum prior to milling, i.e., the spectrum of NH_3, is dominated by peaks at masses 17 and 16. After 1 h of milling, the ammonia peaks are substantially attenuated, a strong signal is observed for H_2 (mass 2), and there is a weak feature at mass 28 indicating N_2 production. If ammonia were simply dissociating to form H_2 and N_2, then the H_2:N_2 peak ratio would be 3:1, rather than the 18:1 ratio observed. It appears that ammonia reacts under milling conditions, with most of the nitrogen binding to the aluminum, eliminating H_2 and a small amount of N_2. After 2 h of milling, there is no significant ammonia left in the headspace. Interestingly, the N_2 peak also disappears, indicating that, under the late-stage milling conditions, i.e., in an atmosphere of mostly H_2, the aluminum surfaces react with or bind N_2 in some fashion.

The fact that no NH_3 is left in the headspace after ≥2 h of milling allows us to calculate the mass fraction of nitrogen in the final particles. From the jar volume (250 mL) and masses of aluminum and tungsten carbide used, we can estimate the headspace volume at ~235 mL; thus, 3.7 atm of NH_3 corresponds to ~0.5 g of nitrogen. Assuming that all the nitrogen is bound to the 2 g of particles formed, nitrogen is seen to make up ~20% of the particle mass. If this nitrogen were all in the form of an AlN layer, and we approximate the actual particle distribution as 75 nm diameter spherical particles, the AlN layer would be ~10 nm thick. Such a thick layer would certainly account for the fact that these particles are not pyrophoric or reactive with water at room temperature.

TGA-MS was performed to look at desorption of products from the samples as a function of temperature. Separate experiments were done using nitrogen and argon as the furnace purge gas, to examine the possibility that aluminum might react with N_2 at elevated temperatures. Figure 3 shows the mass-loss curves for ammonia-milled aluminum particles in both argon and nitrogen gas flows. The sample heated in argon begins to lose mass at ~60 °C, gradually losing ~11% of its mass as the temperature is ramped to 750 °C. The curve for heating in nitrogen is similar, and although there is less net mass loss, there is no obvious signature of nitrogen uptake (see below). The lack of nitrogen uptake indicates that the as-milled particles are passivated with respect to reaction with N_2, even when heated above the bulk aluminum melting point (660 °C).[44]

The other obvious question is what species desorb to account for the relatively large mass losses. The TGA curves show no sharp desorption features, and desorption occurs over a broad temperature range, suggesting either that the desorbing

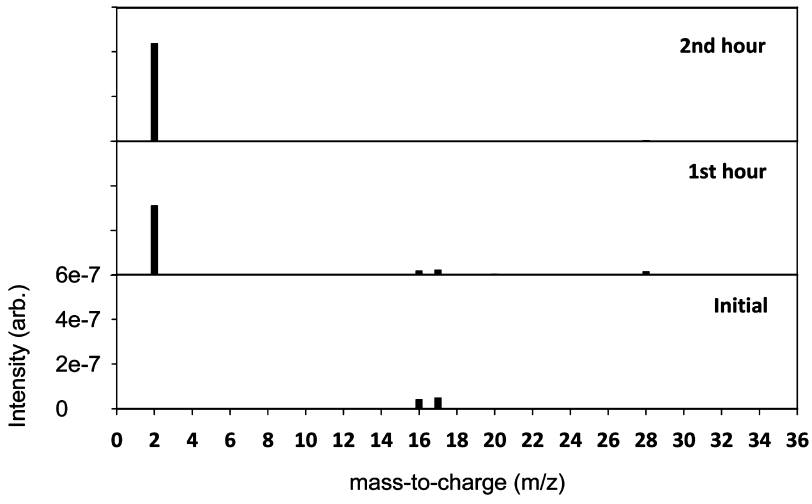

Figure 2. Mass spectrometry of the headspace before and after one and 2 h of milling aluminum in an ammonia atmosphere. Each spectrum was corrected for the instrument background, and the spectra are plotted on the same intensity scale.

DOI: 10.1021/acsami.5b04806
ACS Appl. Mater. Interfaces 2015, 7, 16101−16116

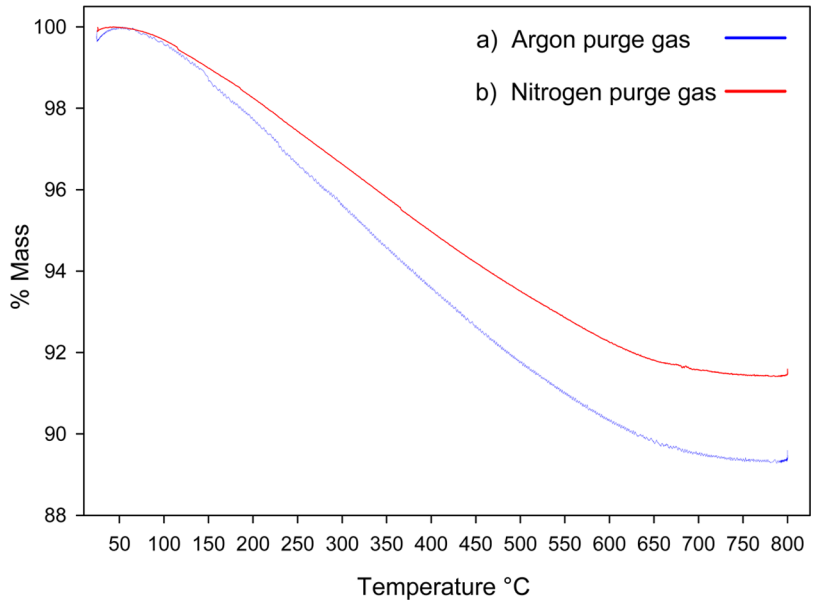

Figure 3. Thermogravimetric analysis of ammonia milled aluminum nanoparticles transferred to a TGA housed in a N_2-filled glovebox, with different exposures to air before analysis.

species have a wide range of binding energies or that they form by decomposition of the thick capping layer on the particles. The temperature dependences of eight masses monitored during TGA (in argon) are shown in Figure S1 of the Supporting Information. The only signals that increase significantly in the temperature range where mass loss is observed are for masses 16, 17, and 18. There is a small desorption feature for mass 18 in the temperature range between ∼50 °C and ∼100 °C, and a much larger feature in the ∼250−600 °C range, both attributed to desorption of water. As shown in Figure 2, the mass spectrum for NH_3 is dominated by signals for masses 17 and 16; thus, those TGA-MS signals are attributed to desorption of NH_3, which shows a sharp onset at 100 °C and continues out to ∼650 °C. Dissociative ionization of water would contribute ∼6% of the mass 17 signal and ∼1% of the mass 16 signal in the range between 250 and 650 °C. Taking dissociative ionization into account, we can estimate that the ∼11% total mass loss results from loss of water amounting to ∼2% of the particle mass, with NH_3 accounting for the remaining ∼9% mass loss.

For both H_2O and NH_3, desorption observed at low temperatures may result from molecularly adsorbed species; however, it is not likely that molecular species would bind strongly enough to persist at high temperatures.[45] Therefore, we attribute the high temperature desorption of these species to recombination reactions of surface functional groups such as $OH_{(ads)}$, $O_{(ads)}$, $H_{(ads)}$, and $NH_{x(ads)}$ in or on the capping layer. There are several likely sources of the oxygen in the NH_3-milled samples, including the oxide layer present on the aluminum feedstock, which may react with H_2 in the late stages of milling to generate $OH_{(ads)}$ and $H_2O_{(ads)}$ that desorb as water during TGA. In addition, the particles are highly hygroscopic and, therefore, likely to adsorb trace H_2O in the atmospheres (and possibly O_2) of the glove boxes used to handle and analyze the particles.

It is useful to consider what the 11% mass loss during TGA implies about the structure of the particle capping layer. If, again, we assume the particles can be represented by 75 nm spherical particles with bulk Al density, there would be an average of $\sim 1.3 \times 10^7$ atoms/particle, with ∼2% ($\sim 2.7 \times 10^5$ atoms) in the surface layer. 11% mass loss in the form of ammonia and water from such a particle corresponds to roughly 8.5 molecules desorbing *per* Al surface site. Even given the uncertainties introduced by distribution of particle size and shape, it is clear that considerably more than a monolayer's worth of NH_3 and H_2O desorbs from the particles.

In TGA, roughly 9% of the particle mass is lost as NH_3, of which $14/17^{ths}$ is N; that is, ∼7.4% of the initial mass is lost in the form of nitrogen. As discussed above, the measured NH_3 consumption during milling implies that the initial total nitrogen content is ∼20 wt %; that is, only ∼40% of the initial nitrogen is lost as NH_3. As noted above, 20% N content would imply a ∼10 nm capping layer if the capping layer were AlN; however, it is clear that the capping layer contains OH, NH_x, and other groups that desorb as H_2O and NH_3 during TGA. The capping layer, therefore, is better described as having $AlN_xO_yH_z$ composition. Upon heating, this layer decomposes to generate NH_3 and H_2O that desorb, leaving behind ∼60% of the initial nitrogen content in some nonvolatile form (e.g., AlN_nO_m).

XPS was used to probe the chemical state of both the nitrogen and aluminum in the capping layer. A sample of the NH_3-milled aluminum particles was transferred to the XPS instrument in an N_2 atmosphere using the manufacturer's inert transfer device, and a survey scan is given in Figure S2, showing the presence of aluminum, nitrogen, oxygen, and carbon. The sensitivity factors for Al, N, O, and C are 0.193, 0.477, 0.711, and 0.296;[46] thus, the O and N signals are significantly exaggerated relative to those for Al in the raw spectrum. Carbon originates from adventitious adsorbates, probably mostly due to the presence of various solvent vapors in our glovebox atmosphere. The signal for oxygen reflects all the sources of oxygen in this experiment, including the oxide layer present on the aluminum feed stock and reaction with contaminants in the glovebox and inert transfer device atmospheres.

High resolution region scans of the Al 2p region are shown in Figure 4, both as-introduced into the XPS vacuum system and

DOI: 10.1021/acsami.5b04806
ACS Appl. Mater. Interfaces 2015, 7, 16101−16116

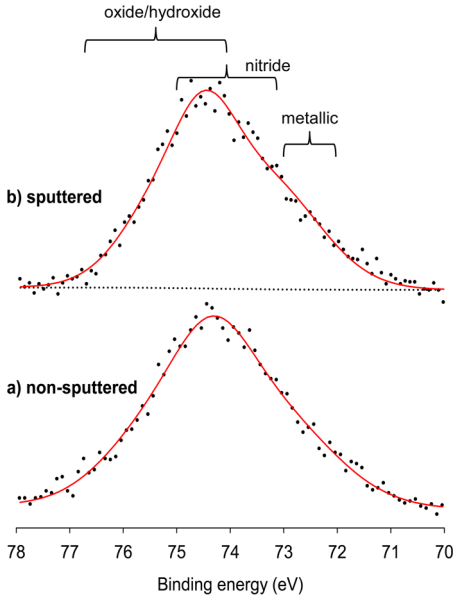

Figure 4. High resolution XPS Al 2p region scan of aluminum nanoparticles milled for 5 h in 55 psia of ammonia (NH_3): a) nonsputtered b) < 5 s argon sputtering.

after sputtering with 4 keV Ar^+ for less than 5 s at ~1 $\mu A/cm^2$ current density, in an attempt to reduce the contributions from adventitious adsorbates. Analogous scans over the N 1s region are shown in Figure 5. The energy scale was corrected for shifts

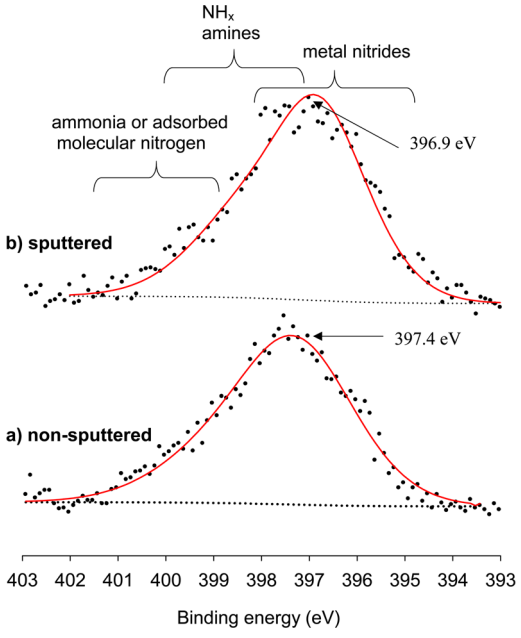

Figure 5. High resolution XPS N 1s region scan of aluminum nanoparticles milled for 5 h in 55 psia of ammonia (NH_3): a) nonsputtered b) < 5 s argon sputtering Note: samples transferred to instrument under argon.

due to sample charging based on the O 1s peak, assumed to be due to aluminum oxide with binding energy of ~531.6 eV. The effective attenuation length[47] for Al photoelectrons in aluminum oxide or aluminum nitride is ~3.2 nm; thus, most of the XPS signal originates from the top 6 to 8 nm of the surface layer. The Al 2p spectrum is much broader than the instrumental resolution (~1 eV fwhm), suggesting that Al in this surface layer is present in a range of chemical states. As indicated on the figure, literature Al 2p binding energies range from 76.7 to 74.1 eV for aluminum oxides and hydroxides,[46,48−56] from ~75 to 73.1 eV for aluminum nitrides,[52,54,57−59] and from ~73 to ~72 eV for metallic Al (Al^0).[33,46,51,54,55,58,60] For the unsputtered sample, the aluminum in the XPS-accessible surface layer is almost entirely oxidized, with binding energies in the range expected for nitrides and oxides/hydroxides, with only a weak tail extending into the range expected for metallic Al. The weakness of the metallic Al signal is not surprising, given the results discussed above, which suggests that the $AlN_xO_yH_z$ capping layer is at least 10 nm thick—enough to almost completely attenuate the signal from the underlying Al particle core. After light sputtering, the metallic Al increased slightly, as might be expected due to sputtering of the surface layer; however, because the sample has many layers of particles present, additional $AlN_xO_yH_z$ is exposed as the top layer of particles is sputtered away.

Figure 5 shows the corresponding N 1s region scans with and without light sputtering. The spectra are broad, again suggesting heterogeneity. The peak value at ~397 eV is consistent with nitride-like nitrogen,[27,46,27,33,61,62] and the tail to high binding energy is consistent with NH_x-like nitrogen.[46] There is a small shift to lower binding energy after light sputtering, possibly indicating Ar^+ impact-induced conversion of NH_x-like nitrogen to more nitride-like bonding. The C 1s and O 1s high resolution spectra are not particularly informative, but are presented, with associated discussion, in the Supporting Information (Figures S3 and S4).

The TGA-MS and XPS results are consistent with NH_3-milled particles being capped with a thick $AlN_xO_yH_z$ layer in which nitrogen is present in both nitride and amine-like states. Amine-like nitrogen on the surface would explain the hygroscopic nature of the particles. As described in the Supporting Information, reaction of the particles with ketones provides further support for amine-like NH_x surface functionality.

B. DFT results for NH_3 interactions with Al_{80}. The structures and energetics of species formed by interaction of NH_3 with aluminum were probed via calculations for an Al_{80} cluster with one or more NH_3 molecules present. Ammonia interacts weakly with the surface of the Al_{80} cluster, henceforth denoted as H_3N:Al_{80}. In order to assess the variability of the binding energies as a function of a specific binding site, four distinct configurations of NH_3 chemisorbed to Al_{80} were computed. These local minima have binding energies ranging from 8 to 16 kcal mol^{-1}, relative to separated Al_{80} + NH_3, and are shown in Figure S11 in the Supporting Information, along with an additional description of the results. The variation in binding energies of NH_3 and the other species discussed below is due in part to the local heterogeneous structure (i.e., "roughness") of the surface of the Al_{80} cluster; however, it is also likely that surfaces formed by fracturing during milling have a variety of sites.

Fragmentation of NH_3. As an initial investigation into the potential chemical reactivity of H_3N:Al_{80}, the energetics were computed for N−H bond dissociation and subsequent covalent binding of the resulting NH_2 and H fragments to Al_{80}, denoted as H_2N−Al_{80}−H. Several local minima of this type were found (Figure S12), bound by 17 to 30 kcal mol^{-1} relative to separated NH_3 + Al_{80}. The greater stability of H_2N−Al_{80}−H

DOI: 10.1021/acsami.5b04806
ACS Appl. Mater. Interfaces 2015, 7, 16101−16116

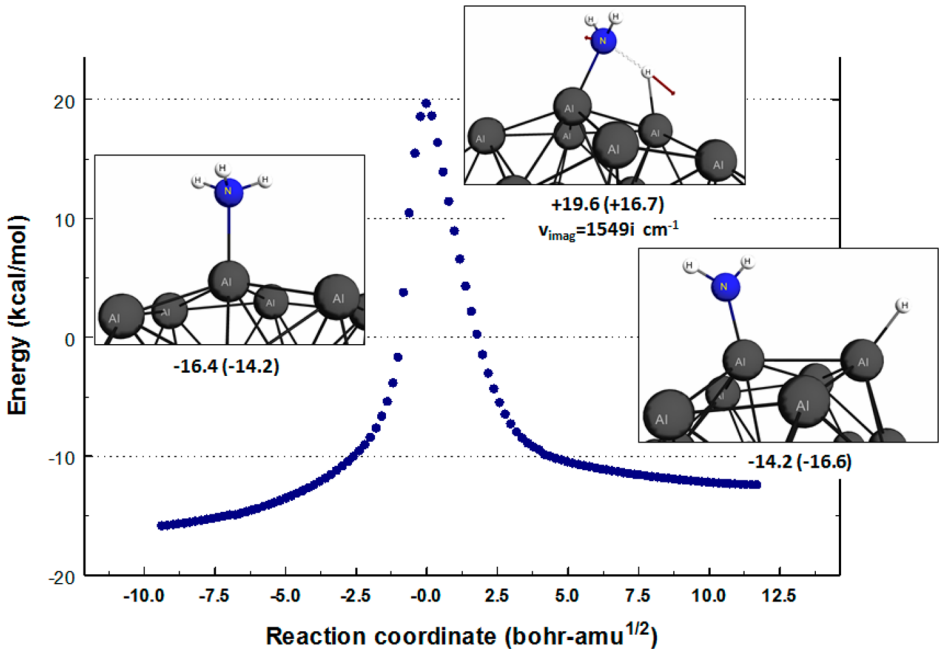

Figure 6. IRC (blue dots) of chemisorbed NH3 undergoing N−H fragmentation to form chemisorbed NH2 + H, excluding zero point energy (ZPE) corrections. The energies, in kcal mol^{-1}, of the stationary points (reactant, saddle point, and product) are relative to separated NH_3 + Al_{80}. ZPE-corrected energies are given in parentheses. A portion of the Al_{80} cluster has been cropped to show the chemisorbed fragments in greater detail.

(17 to 30 kcal mol^{-1}) relative to H_3N:Al_{80} (8 to 16 kcal mol^{-1}) indicates that dissociation of chemisorbed NH_3 to form adsorbed H_2N and H is thermodynamically favored. The products of further N−H fragmentation, leading to chemisorbed NH and N species, are shown in Figures S13 and S14, respectively. As shown, a number of minima were found for NH_{ads} + 2 H_{ads} products with energies 10.6 to 35.4 kcal mol^{-1} below the reactant energy—in the same energy range as those found for NH_{2ads} + H_{ads}. Two minima were found for N_{ads} + 3H_{ads} with energies of 12.6 and 14.5 kcal mol^{-1} with respect to reactants; that is, complete dissociation is energetically uphill compared to NH_{2ads} + H and NH_{ads} + 2H_{ads}.

Since N−H bond dissociation in H_3N:Al_{80} to form H_2N−Al_{80}-H is exothermic, calculations were performed to locate a transition state for this reaction. A saddle point for this reaction was located at 17 kcal mol^{-1} above the NH_3 + Al_{80} reactants, and the reaction path (IRC) is shown in Figures 6 and S15a. The IRC is not corrected for zero-point energy, but for the reactants, transition state, and products, both uncorrected and corrected values are given. Note that the reaction is exothermic by 2 kcal mol^{-1} but that the barrier (31 kcal mol^{-1} with respect to H_3N:Al_{80}) is higher than the barrier for simple desorption of ammonia from H_3N:Al_{80} (14 kcal mol^{-1}). Therefore, desorption of NH_3 has a significantly lower activation energy than N−H dissociation via this saddle point. Note, however, that during milling collisions, adsorbed NH_3 may be trapped and unable to desorb. Furthermore, instantaneous temperatures during energetic collisions can reach 2000 K,[63] driving reactions that would be unlikely under purely thermal conditions. A similar conclusion can be drawn regarding dissociation of adsorbed NH_3 via a structurally distinct but energetically similar saddle point which is shown in Figure S15b, where the reaction is 5 kcal mol^{-1} exothermic but crosses a 30 kcal mol^{-1} barrier.

The reaction enthalpies and barriers for subsequent N−H fragmentation of chemisorbed NH_2-Al_{80}-H to form NH-Al_{80}-2H, as well as the final N−H fragmentation step leading to chemisorbed N-Al_{80}-3H, were also calculated and are described in Figures S16−S18. The barrier heights for these fragmentation reactions, which range from 39 to 62 kcal mol^{-1}, are larger than the 33−35 kcal mol^{-1} barrier for the reverse of the initial fragmentation step (H_2N-Al_{80}-H → H_3N:Al_{80}) and are not considered further.

Formation of H_2. H_2 is produced by milling Al in NH_3 (Figure 2), and several elementary reactions leading to the formation of H_2 were considered. Although we were unable to find a reaction pathway leading to the formation of chemisorbed hydrogen atoms with a barrier less than the energy required for ammonia desorption, it is, nonetheless, possible that such a channel exists. For example, it may be that at the high NH_3 coverages that undoubtedly form during milling under several atmospheres of NH_3, there are lower energy NH_3 dissociation pathways. Therefore, the reaction enthalpy and barrier for recombination of two chemisorbed H atoms to form H_2 were calculated, with the saddle point and IRC shown in Figure S19. This reaction is endothermic by 4 kcal mol^{-1} and has a barrier of 25 kcal mol^{-1}. To assess the mobility of chemisorbed hydrogen atoms on the cluster surface, reaction paths and barriers for migration of a hydrogen atom between aluminum atom binding sites were computed and are shown in Figure S20. The barrier for H atom migration, which ranges from 2 to 17 kcal mol^{-1}, is less than the barrier for recombination (25 kcal mol^{-1}); that is, migration should be facile compared to recombinative desorption of H_2.

The second pathway to H_2 considered is 1,1 elimination of H_2 from the amino group in chemisorbed ammonia, resulting in formation of HN-Al_{80} + H_2. Several unsuccessful attempts were made to locate the saddle point for this process. However, three distinct local minima corresponding to the products formed via this process (HN-Al_{80} + H_2) were located, with binding energies ranging from 7 to 24 kcal mol^{-1} relative to NH_3 + Al_{80} (see Figure S21.) Therefore, with respect to H_3N:Al_{80}, both

DOI: 10.1021/acsami.5b04806
ACS Appl. Mater. Interfaces 2015, 7, 16101−16116

endothermic and exothermic pathways for 1,1 elimination of H_2 are possible, although the barriers are unknown.

Another possible pathway to H_2 might involve reaction of neighboring chemisorbed H and NH_3 (Figure S22), which was found to be endothermic by 1 kcal mol^{-1} with a small barrier of 12 kcal mol^{-1}. A fourth H_2 formation mechanism might involve "bimolecular" elimination of H_2 from adjacent chemisorbed ammonia molecules ($H_3N{:}Al_{80}{:}NH_3 \rightarrow H_2N{-}Al_{80}{-}NH_2 + H_2$). As seen in Figure S23, this reaction is exothermic by 18 kcal mol^{-1}; however, the saddle point located for this reaction lies 28 kcal mol^{-1} above the $2NH_3 + Al_{80}$ asymptote, or more than 50 kcal mol^{-1} above the $H_3N{:}Al_{80}{:}NH_3$ energy. It is, therefore, more energetically favorable for NH_3 to simply desorb, and because H_2 formation via this saddle point is unlikely, the IRC calculations to confirm the corresponding reactants and products were not performed. The final pathway considered is bimolecular H_2 elimination from two chemisorbed NH_2 moieties; i.e., $H_2N{-}Al_{80}{-}NH_2 \rightarrow HN{-}Al_{80}{-}NH + H_2$, which was found to be endothermic by 10 kcal mol^{-1} and for which transition state searches were unsuccessful.

It is important to note that our DFT calculations were limited to a simplified model of the experiments: Al_{80} under conditions of low adsorbate coverage, i.e., at most a few NH_x or H adsorbates/cluster. Given that NH_3 binding to Al_{80} is found to be energetically favorable, it is almost certain that, in the experiments, freshly exposed aluminum surfaces are saturated with NH_3 (or fragments thereof), which may significantly change the energetics for NH_3 adsorption, dissociative chemisorption, and bimolecular reactions between neighboring adsorbates. For example, in the limit of low coverage, diffusion of H atoms away from dissociatively adsorbed NH_{3-x} would tend to make the dissociative adsorption process irreversible; however, under saturation conditions, the H atoms may simply recombine with neighboring NH_{3-x} adsorbates. If H atoms recombine and desorb as H_2, this will tend to make dissociative adsorption of NH_3 irreversible, provided that H_2 does not readily undergo dissociative adsorption. The fact that NH_3 is consumed and H_2 produced during milling suggests that NH_3 dissociative adsorption is, in essence, irreversible. As milling continues, a relatively thick $AlN_xO_yH_z$ layer forms, indicating that reactions continue well beyond the point of simply producing a saturated monolayer on the Al surface. While it is impractical to include high coverages, impurities, etc. in the DFT model, the results, nonetheless, provide insight into the initial reactions of NH_3 on aluminum surfaces.

In summary, the DFT calculations show that adsorption of NH_3 on aluminum is energetically favorable and that dissociation to chemisorbed NH_2 + H or NH + 2H can be exothermic, although we were not able to find transition states with energies below the desorption energy of $H_3N{-}Al_{80}$. Similarly, reaction pathways for H_2 formation were found that are exothermic (i.e., 1,1 elimination from chemisorbed NH_3 and bimolecular elimination from two NH_3 molecules) or that have a modest barrier (recombination of two chemisorbed H atoms or elimination from coadsorbed H and NH_3). Although the complexity of the system precludes exhaustive searches of the large number of potential adsorption geometries and reaction paths, consideration of the DFT and experimental results suggests that the initial species formed in interaction of NH_3 with aluminum are chemisorbed NH_3, NH_2, and H. In addition, as discussed further in the Supporting Information, formation of N_2, N_2H_2, and N_2H_4 via the recombination of chemisorbed species such as H, N, NH, and NH_2 is a highly endothermic process (+42, +103, and +80 kcal mol^{-1}, respectively, as shown in Figure S24). This finding is consistent with the experimental observation of H_2 as the predominant gaseous product, with minimal N_2 production in the ball milling experiments.

C. Aluminum particles produced by milling in MMA. While the fact that ammonia serves as an efficient size-reduction agent in aluminum ball milling is interesting, the observation that the resulting particles are heavily passivated by a thick $AlN_xO_yH_z$ layer makes the particles less interesting from the fuels perspective. Particles produced in monomethylamine (MMA) atmospheres are more promising. As noted, the MMA vapor pressure is only ~2 atm, and to compensate for the lower initial concentration of reactive gas present, the jar was evacuated and refilled with fresh MMA after each hour of milling. After 4 h, the result was conversion of the initial ~2 g of millimeter aluminum flakes to a homogeneous dark black powder that resembled the ammonia-milled particles. Unlike the ammonia-milled samples, however, these particles were pyrophoric and autoigniting within a few seconds upon air exposure. Higher reactivity suggests that MMA milling results in less thoroughly passivated particles than milling in NH_3, but it is also conceivable that the MMA-milled samples simply contain more small particles, which tend to autoignite more readily because they have less bulk to dissipate heat generated by surface reactions.

The particle size distribution was measured by DLS, after dispersing the particles in acetonitrile, and the result is shown in Figure 7. The size distribution was bimodal, with a "small particle" mode in the 100 to 200 nm range accounting for ~63% of the particle mass, with the balance in a mode ranging from ~450 to 900 nm. SEM of these particles (Figure 7, inset) shows what appear to be primary particles in the size range between ~60 nm and ~300 nm, with a few ranging up to ~500 nm in size. The particles look relatively smooth but are elongated and appear somewhat flattened. Given the lack of shape sensitivity of DLS, the agreement with SEM is reasonable and suggests that the ~450–900 nm mode seen in DLS consists of aggregates. Both SEM and DLS measurements indicate that the particles produced by MMA milling are somewhat larger than those produced in NH_3. We, therefore, conclude that the substantially higher reactivity observed for MMA-milled particles is a result of less passivated surfaces, compared to particles produced by NH_3-milling.

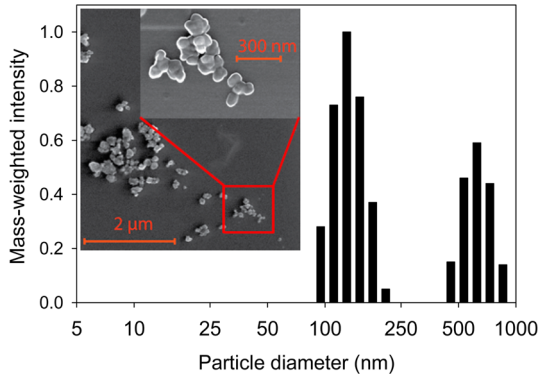

Figure 7. Dynamic light scattering measurement for MMA-milled aluminum particles in acetonitrile suspension. Inset: SEM image of particles.

DOI: 10.1021/acsami.5b04806
ACS Appl. Mater. Interfaces 2015, 7, 16101–16116

Headspace analysis was performed after each hour of milling in MMA, and the results are presented in Figure 8. The MMA

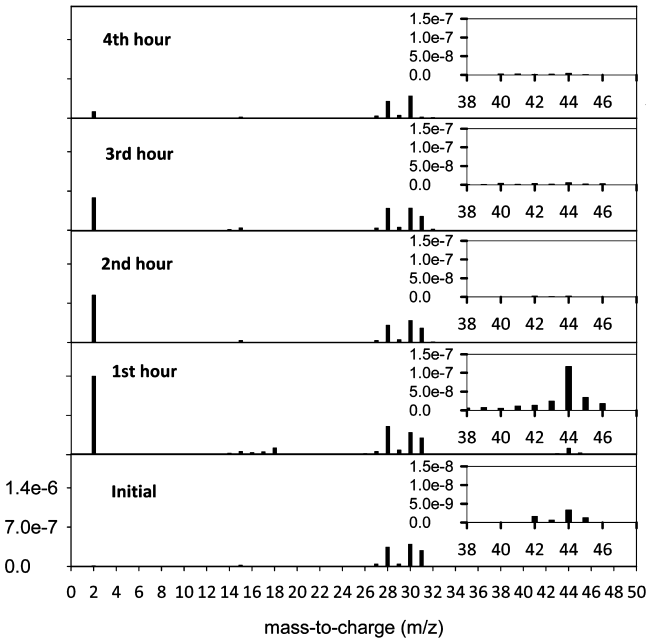

Figure 8. Mass spectrometric analysis of the headspace during milling of aluminum in MMA. Note that the jar was evacuated and refilled with MMA prior to each hours milling. All spectra are scaled to constant intensity of m/z = 30.

molecular mass is 31; however, the largest peak in the MMA mass spectrum is mass 30, and to account for fill-to-fill variation in the MMA pressure, each spectrum has been normalized to constant mass 30 intensity. The "initial" mass spectrum is for MMA prior to milling and is in good agreement with the literature spectrum for MMA,[64] with the exception that there are a number of barely detectable peaks in the mass 40 to 45 range (see inset), which match reasonably well to the expected intensity pattern for dimethylamine.[65] Apparently the MMA gas either had dimethylamine contamination on the order of 1% or reacted upon introduction to the milling jar to produce it.

After 1 h of milling, the spectrum is dominated by mass 2, indicating significant H_2 production, and by peaks due to residual MMA (recall that the spectra are normalized to constant mass 30 intensity). During the second hour of milling (after evacuating the jar, and refilling with fresh MMA), H_2 was again the major gaseous product. Indeed, the only significant signals in the second hour spectrum were for H_2 and residual MMA (the mass 15 peak is from dissociative ionization of MMA). The amount of H_2 produced during each hour of milling clearly declined with time, such that, by the fourth hour, there is little evidence of reaction, and only unreacted MMA is present. Given that MMA appears to react with fresh aluminum surfaces generated during size reduction, the implication is that the net production of new surface area declines after 2 to 3 h of milling.

In addition to H_2 and residual MMA, the first hour spectrum shows evidence of a number of other gaseous species. The fact that these peaks are absent in later spectra suggests that their source is contaminants introduced on the surfaces of the aluminum feedstock or milling media, such that they are lost when the jar is evacuated and refilled after the first hour. While these are minor products, considering their origins provides some insight into the chemistry occurring during milling. Mass 46 almost has to be either $C_2H_6O^+$ or N_2O^+, and in the former case there would also be a contribution to mass 45. The high intensity at 44 suggests CO_2. Hydrocarbon contaminants (e.g., hexane used for media and jar cleaning) would crack in the ionizer to give a variety of $C_nH_m^+$ ions, although it should be noted that ionizer cracking of higher hydrocarbons cannot account for the enhanced signal at masses 44 and 28, or the peaks at masses 16 through 18. The increase, compared to the MMA spectrum, in the relative intensity of mass 28 in the first hour spectrum is too large to explain as CO^+ from CO_2, and thus it suggests production of a small amount of N_2, as was seen after the first hour of NH_3 milling. The small peaks at masses 12−18 are partly attributable to dissociative ionization of MMA and dimethylamine; however, there also appears to be some production of methane and water. Methane formation might be expected to accompany N_2 production, and as shown next, both methane and water desorb from the MMA-milled particles when they are heated.

As with the ammonia-milled samples, mass spectrometry was used to probe gases desorbing from a particle sample as it was heated. Because the number of potential products is higher for MMA, and the TGA-MS instrument only allows a limited number of peaks to be monitored, we first examined full desorption mass spectra for temperatures up to 300 °C, in order to identify products via fragmentation patterns and to choose peaks for TGA-MS analysis. For this measurement, ∼250 mg of particles were collected from the jar after the fourth milling hour and transferred to a vial in the glovebox. The vial was attached to the inlet of the same mass spectrometer used for the headspace analysis, evacuated to remove the glovebox N_2, resealed, and then stepped through a series of temperatures, taking a mass spectrum of the desorbed gases after temperature equilibration (Figure 9). For reference,

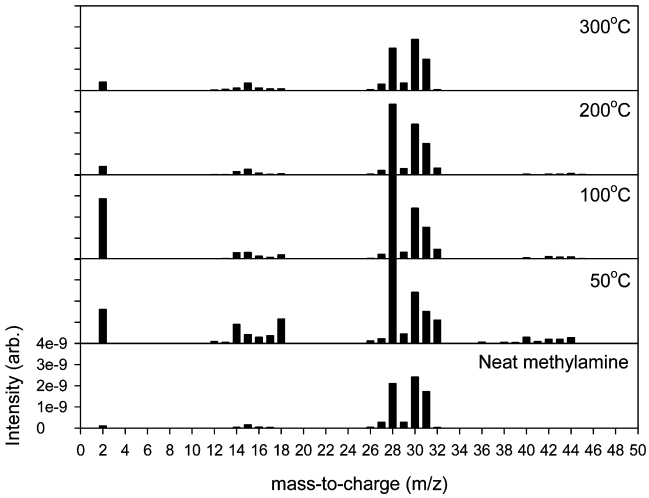

Figure 9. Thermal desorption mass spectral analysis of MMA-milled aluminum particles.

the spectrum of neat MMA is shown at the bottom of the figure. At 50 °C, there is already significant signal for products desorbing from the sample. The mass 28 peak, which was allowed to go off scale, is attributed mostly to residual glovebox N_2, which also contributes to mass 14. Those peaks aside, the mass pattern can be assigned to the following desorbing species, in descending order of importance: MMA, H_2, water,

DOI: 10.1021/acsami.5b04806
ACS Appl. Mater. Interfaces 2015, 7, 16101−16116

methane, and dimethylamine. There is also a peak at mass 32, only a few percent of which can be attributed to $^{13}CH_3NH_2$, suggesting the presence of O_2. Given that these particles are reactive enough with oxygen to be pyrophoric in air, it would be surprising if free O_2 could exist in the sample. More likely, O_2 may have outgassed from the gas line connecting the sample vial to the mass spectrometer inlet. The H_2 signal peaks at 100 °C, and by that point, the water, O_2, N_2, methane, and dimethylamine signals decrease substantially. The H_2 signal decreases sharply at 200 °C and above, such that the dominant desorption signal is for MMA, with only small amounts of H_2, water, and methane remaining at 300 °C.

The TGA results for MMA-milled aluminum particles in both N_2 and Ar purge gases are shown in Figure 10. Mass loss

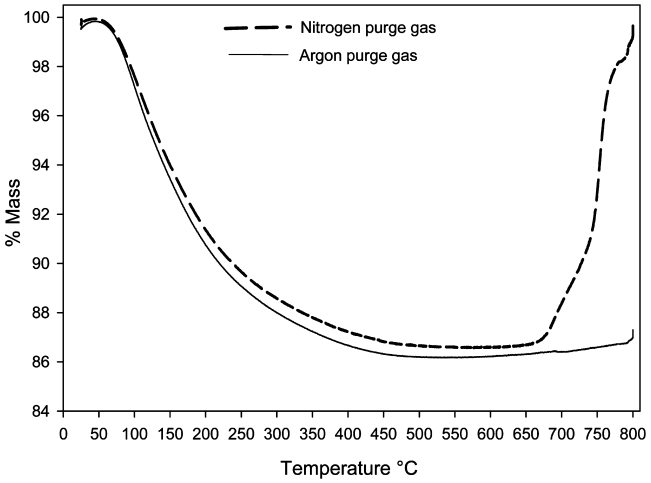

Figure 10. Thermogravimetric analysis of methylamine milled aluminum nanoparticles transferred to a TGA housed in a N_2-filled glovebox.

begins at ~60 °C and reaches ~13% by ~500 °C, compared to ~11% mass loss by ~650 °C for NH_3-milled particles (Figure 3). While the results are superficially similar for the NH_3- and MMA-milled particles, it is important to note that 80% of the mass loss for the MMA-milled particles occurs below 250 °C, compared to ~525 °C for the NH_3-milled particles. Clearly the capping layer is more weakly bound in the MMA case. More obviously, when N_2 is used as the purge gas, the MMA-milled particles show rapid mass gain starting near the melting point of bulk aluminum (660 °C). The small mass gain noted for Ar furnace gas is attributed to infiltration of N_2 from the surrounding glovebox into the TGA. The mass gain presumably indicates reaction to form some thermally stable aluminum−nitrogen compound.

During TGA, the intensities of the mass peaks at 2, 14, 15, 16, 17, 18, 26, 27, 28, 29, 30, 31, and 32 were monitored as a function of temperature, and this data set is given in Figures S25 and S26. Masses 30 and 31,which are major peaks for ionization of MMA (see Figure 9, bottom) show a desorption feature with onset near 50 °C, peak near 100 °C, and ending near 250 °C. As required if MMA is, indeed, the main desorption product, all the other minor peaks expected for MMA ionization (14, 15, 26, and 32 = $^{13}CH_3NH_2$) also show a similar desorption feature. Mass 28, which is also a major MMA mass spectral peak, has such high background in the mass spectrometer that it is impossible to observe any increase from desorbing MMA. Mass 18, which is attributed to water desorption, also shows a similar desorption feature, and the mass 16 and 17 signals, therefore, must have contributions from both MMA and water desorption.

The only mass showing a significantly different desorption temperature dependence is mass 29. This mass shows a minor feature at low temperatures, as expected from dissociative ionization of desorbing MMA, but also a major feature starting at ~375 °C, which is not seen for any of the other masses associated with MMA desorption. The mass 29 ion is almost certainly $CH_2{=}NH^+$, suggesting that the molecule desorbing at high temperatures is methanimine, i.e., MMA which has lost H_2. This desorption channel was not seen in the mass spectra in Figure 9 because we were not able to reach high enough temperatures with the glass sample vial. It is not clear if desorption of this mass above 375 °C indicates that $CH_2{=}NH$ is bound strongly to the surface, if 375 °C is the temperature where strongly adsorbed MMA begins to dehydrogenate, or if $CH_2{=}NH$ is produced by decomposition of an $AlC_nH_mN_xH_y$ capping layer. Unfortunately, the high background/low sensitivity of the TGA-MS for mass 2 precludes looking to see if H_2 and $CH_2{=}NH$ desorption are correlated.

Because of the extensive fragmentation of MMA, and high background at some masses of interest, there is considerable uncertainty in the integrated desorption intensities; however, we can say that water, MMA, and methanimine are the main desorption products. MMA and water, which desorb with roughly equal intensities, mostly in the 50−250 °C range, account for ~90% of the total mass loss, with the balance due to methanimine desorbing above 375 °C.

As with the NH_3-milled particles, FTIR characterization failed; however, XPS provides some insight into the nature of the MMA capping layer. As might be expected from the lower desorption temperatures seen for the MMA-milled sample in TGA, this sample was found to outgas badly in vacuum, and it was necessary to degas the sample before introduction into the ultrahigh vacuum chamber. A sample was prepared and loaded into the XPS inert transfer device in the glovebox, and then the transfer device was attached to a small vacuum chamber with a base pressure of $\sim 3 \times 10^{-8}$ Torr. The transfer device was then opened in this chamber (leading to an increase in pressure to 1×10^{-7} Torr) and allowed to pump until the pressure had decreased back to baseline, which took ~2 days. At that point, the transfer device was sealed, pressurized with Ar, and transferred to the XPS instrument. XPS was obtained immediately after transfer to the instrument, and then to examine the effects of deliberate air exposure, the sample was moved into the XPS instrument load-lock chamber, briefly exposed to laboratory air, and then pumped down and reintroduced to the XPS analysis chamber. The post-exposure XPS was done using a different area on the sample to avoid potential X-ray damage artifacts. Peak energies were adjusted using the C 1s adventitious peak at 284.8 eV for the air-exposed sample.

The Al 2p spectra for this sample are presented in Figure 11. In comparison to the Al 2p spectrum for NH_3-milled aluminum, the as-transferred ("Inert") spectrum is considerably sharper, with a distinct peak around 72 eV, attributed to Al^0 in the particle core, and a somewhat broader peak near 74.5 eV in the range expected for aluminum oxides and nitrides.[41,48,52,53] The distinct peak for Al^0 suggests that the capping layer is thinner on the MMA-milled particles, although the nitride/oxide component still dominates the spectrum. The effect of air exposure was modest, mostly appearing as a broadening of the

DOI: 10.1021/acsami.5b04806
ACS Appl. Mater. Interfaces 2015, 7, 16101−16116

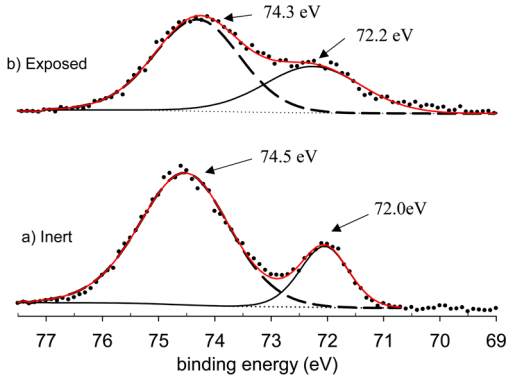

Figure 11. High resolution X-ray photoelectron Al 2p region scan of particles milled in methylamine for 4 h, and transferred to the XPS instrument under argon. a) As-transfer b) exposed to air.

metallic aluminum peak in the "Exposed" spectrum. Since we know that freshly milled samples of this material are pyrophoric, the small effect observed for air exposure in the instrument load lock probably indicates that the sample had already received significant exposure to oxidizing contaminants during preparation in the glovebox, degassing, and transfer to the XPS instrument, and thus was already largely passivated.

The N 1s spectra presented in Figure 12 also show signs that the MMA capping layer is quite different than that formed by

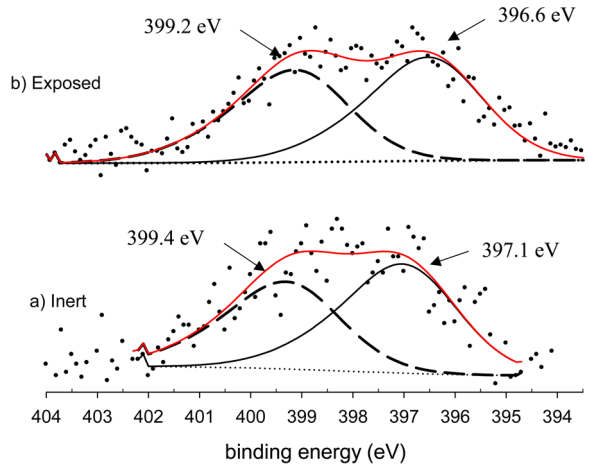

Figure 12. High resolution X-ray photoelectron N 1s region scan of particles milled in methylamine for 4 h, pressed into a pellet, and transferred to the XPS instrument under argon: a) as transferred in inert atmosphere, b) exposed to air.

NH_3 milling. The higher binding energy N 1s component, peaking near 399 eV, is in the range expected for organic nitrogen[62,66] and is consistent with the observation that intact MMA (and dimethylamine and CH_2NH) desorbs from this material starting at quite low temperatures. For comparison, the NH_3-milled sample (Figure 5) shows no distinct feature in this high binding energy range. The lower binding energy component, peaking near 397 (~0.5 eV lower than the peak for NH_3-milled aluminum), is consistent with binding energies reported for metal nitrides.

The other major difference is that the amount of nitrogen in the surface layer of the MMA-milled particles is smaller than that for the NH_3-milled sample, as can be inferred by comparing the signal-to-noise ratios of the spectra in Figures 5 and 12. Integration of the background-subtracted spectra shows, in fact, that the XPS-visible N 1s signal is 6 times smaller for the MMA-milled sample. Given the estimate, from NH_3 consumption, that the capping layer on the NH_3-milled particles is ~10 nm thick (treated as AlN), the XPS results suggest that the analogous thickness for MMA-milled particles is in the ~2 nm range. Furthermore, the observation that intact MMA desorbs from these particles at low temperatures suggests that a significant fraction is simply molecularly adsorbed to the surface of the particles, and this conclusion is supported by the presence of the high binding energy N 1s component in Figure 12.

After air exposure, the spectrum broadens and shifts slightly to lower binding energy, but the relative intensities of the high and low binding energy components are unchanged, presumably reflecting the unavoidable oxygen exposure even in the inert-transferred sample. C 1s and O 1s region spectra for the as-transferred and air-exposed samples are presented in Figures S27 and S28. Perhaps the only point of interest is that the O 1s intensity does not increase significantly after air exposure, again consistent with the idea that the sample was already largely passivated by reaction with oxidizing contaminants in the glovebox and inert transfer device atmospheres.

D. DFT results for CH_3NH_2 + Al_{80}. Similar to the case of ammonia, monomethylamine forms a weak dative bond to the surface of the Al_{80} cluster with a binding energy of 18 kcal/mol, with structure illustrated in Figure S29. Starting from this structure, three bond dissociation pathways (N−H, C−H, and C−N bond scissions) of chemisorbed monomethylamine, denoted henceforth as MMA:Al_{80}, were considered. The final products of these three reactions are shown in Figure 13. Dissociation of an N−H bond to form chemisorbed CH_3NH and H (CH_3NH-Al_{80}-H; see Figure 13a) is exothermic by 8 kcal mol^{-1} relative to MMA:Al_{80}. C−H bond dissociation leading to formation of (CH_2NH_2)-Al_{80}-H (Figure 13b) is endothermic by 2 kcal mol^{-1} with respect to MMA:Al_{80}. In contrast, cleavage of the C−N bond to form CH_3-Al_{80}-NH_2 (Figure 13c) is exothermic by 26 kcal mol^{-1} and therefore the most thermodynamically favorable of the three bond dissociation reactions. Additional isomers, with energetics, for the dissociation products CH_3NH-Al_{80}-H, (CH_2NH_2)-Al_{80}-H, and CH_3−Al_{80}-NH_2 are shown in Figure S30.

Saddle points were found for N−H and C−H fragmentation in MMA:Al_{80}, as shown in Figures S31 and S32. Although calculations to locate the saddle point for C−N bond fragmentation in MMA:Al_{80} to produce CH_3−Al_{80}-NH_2 were unsuccessful, a transition state leading to formation of the latter from (CH_2NH_2)-Al_{80}-H was located and is shown in Figure S33. Of these three pathways, N−H fragmentation has the lowest barrier (26 kcal mol^{-1}.) Nonetheless, the corresponding saddle point is 8 kcal mol^{-1} higher in energy than separated MMA + Al_{80}, indicating that simple desorption of CH_3NH_2 from MMA:Al_{80} is a more favorable process than N−H fragmentation. As discussed above, however, under the instantaneous conditions arising during milling collisions, it is not unlikely that high energy reaction channels may be significant.

Formation of H_2. Several pathways leading to formation of H_2 were considered, including (a) H_2 elimination from chemisorbed CH_3 and NH_2, unimolecular H_2 elimination from MMA:Al_{80}, and (c) bimolecular H_2 elimination from neighboring chemisorbed MMA molecules, MMA:Al_{80}:MMA (see Figures S34−S35.) Only in the latter instance were

DOI: 10.1021/acsami.5b04806
ACS Appl. Mater. Interfaces 2015, 7, 16101−16116

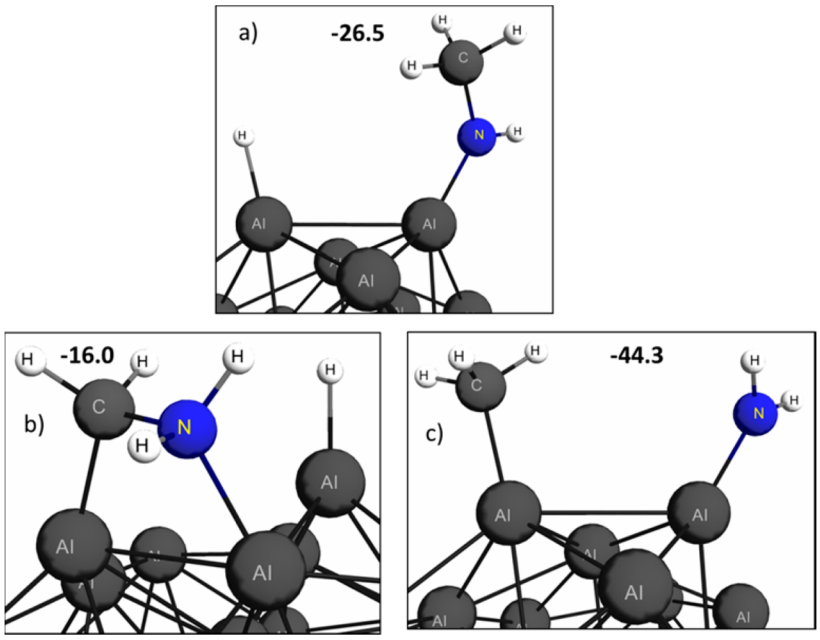

Figure 13. DFT optimized structures of products resulting from bond dissociation of methylamine chemisorbed on Al_{80}. Chemisorbed products following N−H bond scission (panel a), C−H bond scission (panel b), and C−N bond scission (panel c.) Binding energies are relative CH3NH2 + Al_{80}. ZPE-corrected energies are given in parentheses. Portions of the Al_{80} cluster have been cropped to show the chemisorbed fragments in greater detail.

exothermic pathways found, with the reaction CH_3NH_2:Al_{80}:NH_2CH_3 → CH_3NH-Al_{80}-$NHCH_3$ + H_2 having the largest exothermicity, 17 kcal mol^{-1}, and thus representing the most probable means of H_2 formation.

Formation of CH_2═NH. As shown above, there is evidence for desorption of methanimine (CH_2NH) above 375 °C, and as discussed in the Supporting Information, the calculated reaction enthalpy to form chemisorbed CH_2═NH via a concerted 1,2 elimination of H_2 from MMA:Al_{80} is endothermic by 28 kcal mol^{-1}, i.e., well above the desorption energy for intact MMA (see Figure S34b.) In contrast, stepwise H atom elimination, shown in Figure S36, resulting in formation of CH_2═NH:Al_{80}-2H is endothermic by only 17 kcal mol^{-1}, which is slightly less than the energy required for intact desorption of MMA (18 kcal mol^{-1}). Regarding the two possible stepwise pathways shown in Figure S36, the one occurring via initial C−H fragmentation (panel a) must traverse a barrier of 50 kcal mol^{-1}, as illustrated in Figure S32. In contrast, the stepwise pathway via initial N−H fragmentation (panel b in Figure S36) presumably has a barrier similar to that of the reaction pathway illustrated in Figure S31 (26 kcal mol^{-1}). The latter pathway provides an energetically reasonable mechanism for production of CH_2═NH, assuming that the unknown barrier for elimination of the second H atom (i.e., CH_3NH-Al_{80}-H → CH_2═NH:Al_{80}-2H) is not excessively large. Furthermore, the two adsorbed H atoms can undergo recombinative desorption at high temperatures, providing an additional route to the major H_2 product.

Formation of CH_3NHCH_3. Three elementary bimolecular reactions leading to the formation of chemisorbed dimethylamine (DMA:Al_{80}) were considered and are described in the Supporting Information (see Figures S37−S39). Of these, only one is exothermic (17 kcal mol^{-1}, involving the migration of a methyl group from chemisorbed MMA to a neighboring chemisorbed −$NHCH_3$ group, resulting in formation of H_2N−Al_{80}:DMA).

Formation of NH_3, CH_4, and CH_3CH_3. The most direct and plausible routes to formation of NH_3 and CH_4 are via recombination of chemisorbed NH_2 + H and CH_3+ H, respectively. However, a facile pathway leading to chemisorbed NH_2 or CH_3 starting from MMA:Al_{80} has not been found. Although formation of chemisorbed NH_2 and CH_3 could occur by the two-step process described earlier, namely, initial C−H fragmentation in MMA:Al_{80} (Figure S32) followed by C−N fragmentation of chemisorbed CH_2NH_2 (Figure S33), the first step in this process must traverse a large barrier of 50 kcal mol^{-1} and, therefore, is unlikely to occur to a significant extent. Even if chemisorbed CH_3 were present on the aluminum surface, recombination with a chemisorbed H atom to produce CH_4 has a calculated barrier of 43 kcal mol^{-1}, as shown in Figure S40, presumably accounting for the minor amount of CH_3 observed.

Similarly, since the most straightforward route to formation of ethane is via recombination of chemisorbed CH_3 fragments, the absence of ethane as a product is likewise consistent with the unlikelihood of forming chemisorbed CH_3. Although recombination of two chemisorbed methyl groups to produce ethane is endothermic by only 7−15 kcal mol^{-1}, the barrier for this process is unknown.

In summary, the DFT calculations show that adsorption of MMA onto aluminum is energetically favorable, with little or no activation energy. Reactions leading to products such as H_2, CH_2═NH, dimethylamine, and other products were found to be exothermic, or with endothermicity in a range accessible at milling temperatures ($T_{average}$ < ∼380 K). Many of these processes were found to have high activation barriers, however, and we did not identify obvious pathways to many of the observed products. Again, however, we emphasize that the DFT calculations were done in the limit of very low adsorbate coverage. Under the experimental conditions, we expect that the surfaces should be saturated by MMA, which is likely to change the energetics for some of the decomposition reactions

DOI: 10.1021/acsami.5b04806
ACS Appl. Mater. Interfaces 2015, 7, 16101−16116

and possibly open new reaction pathways. In addition, the high instantaneous temperatures reached during energetic collisions in the mill[63] may drive reactions that would be unlikely under purely thermal conditions.

IV. CONCLUSIONS

We previously demonstrated that aluminum particles in the 100 nm size range can be produced by milling in liquid reagents or solutions thereof, which bind to newly created surfaces, lowering the free energy of surface creation and reducing the tendency toward cold-welding.[26] Milling in liquids that do not bind strongly to aluminum (e.g., alkanes) resulted in no particle production. The best liquid milling agent found was neat acetonitrile, which resulted in efficient particle production, but with roughly equal masses of nanoparticles and micron scale particles. We also examined milling with oleic acid and solutions thereof, and in liquid amines (oleylamine and benzylamine), and found that while there was efficient production of particles, at most 10% of the product mass was nanoparticles. In contrast, we have shown above that milling in gaseous amines results in rapid and exclusive production of particles, mostly in the 40−100 nm range for NH_3 and in the 100−250 nm range for MMA. As also discussed above, milling in H_2, Ar, or N_2 atmospheres resulted in no particle production but rather lead to cold welding of the aluminum flake feedstock to form 1 to 2 mm diameter spheres.

The much more efficient size reduction in gaseous amines, compared to liquid milling agents, may be influenced by effects such as surface lubrication and evaporative cooling by the liquids; however, we propose that the high molecular velocities and low viscosity of small gaseous reactant molecules are also quite important. Their high diffusion speeds mean that a high density of reactant molecules is present at internal surfaces of cracks formed by milling impacts, adsorbing and thereby reducing the energy required to propagate the cracks (*vide infra*). For viscous liquids or liquid solutions, delivery of the surface-active molecules to the crack tip may be slow, and for bulky molecules (e.g., oleic acid), steric effects will also limit the coverage. Its small size may explain why neat acetonitrile was the best liquid agent found for Al nanoparticle production.

Consider the equilibrium for molecularly adsorbed NH_3 and MMA on aluminum surfaces. The collision rate for NH_3 under the conditions present when milling started (∼3 atm, 350 K) is $\sim 10^9\ s^{-1}$ *per* surface aluminum atom, and the analogous rate for MMA is $\sim 4 \times 10^8\ s^{-1}$. Given the calculated binding energies (E_{des}), ranging from ∼8 to ∼18 kcal/mol depending on binding site, and assuming barrierless first order desorption ($k_{des} = \nu \exp(-E_{des}/kT)$), with $\nu \approx 10^{14}\ s^{-1}$, we can estimate that the desorption rates will range from $\sim 10^9\ s^{-1}$ to $\sim 10^3\ s^{-1}$ over the range of binding energies. The ratio of the collision and desorption rates implies that the steady state occupancy will be substantial, even for the weakest binding sites, and that the stronger binding sites will essentially be saturated within nanoseconds of their initial exposure to the milling gases.

The process of converting millimeter flakes to 100 nm particles with aspect ratios similar to those shown in Figures 1 and 7 creates roughly ∼25 m^2 of new surface area *per* gram of particles. The free energies of aluminum surfaces such as Al(111), Al(110), and Al(210) are reported to be in the range of 1.14 to 1.16 J/m^2,[67−69] and high index/defective surfaces produced by milling are likely to have somewhat higher energies.[70] 1.16 J/m^2 corresponds to ∼0.55 eV/surface atom, or ∼12.7 kcal/mol of surface atoms. As discussed above, the calculated energy of the NH_3:Al_{80} dative bond varies from 8 to 16 kcal/mol, and the MMA:Al_{80} bond is ∼18 kcal/mol. The degree to which adsorption can compensate for the energy required to create new Al surface area depends on the coverage. The calculated structures (Figures S11, S22, S29, and S35) suggest that the maximum coverage might approach ∼0.25 to 0.5 NH_3 or MMA molecules per Al atom, and such coverages are also consistent with comparison of the effective van der Waals diameter of NH_3 (∼4 Å),[71] and the Al−Al spacings, which are 2.86 and 4.04 Å for the (110) surface,[72] for example. In addition to adsorption of intact NH_3 and MMA, however, the production of H_2 and other minor gaseous products during milling suggests that dissociative adsorption must also occur, and this process should result in not only higher coverage but also higher binding energies. For example, our calculations show that NH_2 and H adsorb to neighboring Al atoms with net binding energy of up to ∼30 kcal/mol—more than enough to essentially cancel the energy cost of creating new surface area. The high adsorption energies, and the fact that both NH_3 and MMA are gases able to rapidly penetrate small cracks, presumably accounts for why both are such effective milling agents.

The DFT calculations found that adsorption of intact NH_3 and MMA is exoergic and that a variety of dissociative adsorption processes are also exoergic; however, we were unable to find low energy transition states leading to these adsorbed decomposition products. Nonetheless, it is clear that there is substantial decomposition of the adsorbed reactants, as shown by copious production of H_2 during milling, and XPS and TGA results showing that the particles are capped with a few nanometers of some material containing aluminum with nitride-like Al 2p binding energy, and nitrogen with both nitride and organic nitrogen-like N 1s binding energies. Under the high coverages and extreme instantaneous temperature conditions generated in milling, there evidently are efficient decomposition pathways.

The mass and temperature data from TGA provide additional insight into the nature of the particle capping layers. Both NH_3- and MMA-milled particles undergo loss of 10%−13% of their initial masses, corresponding to a few monolayers worth of material desorbing. In both cases, the reactants themselves, i.e., NH_3 or MMA, are major desorption products, although there is also water for the ammonia-milled particles (Figures 3 and S1), and CH_2NH (Figures S25−S26) and H_2 (Figure 9) for the MMA-milled particles. H_2 may also be evolved by the NH_3-milled sample, but we were unable to monitor its mass in the TGA-MS experiment.

While the desorption behavior is superficially similar for NH_3- and MMA-milled particles, the temperature dependence of the desorption is quite different. As shown in Figures 3 and 10, mass loss in both cases begins at 60−70 °C; however, for the MMA-milled particles, ∼80% of the mass loss occurs below ∼250 °C, while, for the NH_3-milled particles, only ∼27% of the mass loss occurs below 250 °C, and 80% loss requires heating to ∼525 °C.

The XPS results for the two samples are also different, and they suggest an explanation for the differences in desorption behavior. For the NH_3-milled particles, there is relatively little XPS signal arising from Al^0 in the particle cores, and there is a strong N 1s signal, mostly corresponding to some nitride-like state. The TGA and XPS results suggest that the particles are capped with a thick layer of some $AlN_xO_yH_z$ composition, with additional NH_3 molecularly adsorbed on the surfaces. When

DOI: 10.1021/acsami.5b04806
ACS Appl. Mater. Interfaces 2015, 7, 16101−16116

heated, such a layer would tend to evolve molecularly adsorbed NH_3 at low temperatures and then produce NH_3 and H_2O by decomposition of the $AlN_xO_yH_z$ layer at high temperatures, as is observed. The observed weakness of the XPS Al^0 signal is consistent with a thick capping layer, given the ~3.2 nm effective attenuation length[47] for Al photoelectrons in alumina or AlN, and the thick capping layer also passivates the particles with respect to autoignition in air and toward reaction with N_2 at high temperatures.

For the MMA-milled particles, XPS shows higher Al^0 signal from the particle cores compared to the NH_3-milled case, and the nitrogen signal is roughly equal divided between nitride-like and amine-like binding energies. The MMA-milled particles are also moderately pyrophoric, and they react with N_2 above 650 °C. The total mass loss is quite similar to that of the NH_3-milled particles, but it occurs at much lower temperatures. We interpret these results to indicate the presence of a relatively thin layer of fully passivated nitride-like aluminum, with a substantial amount of MMA molecularly adsorbed on its surface. A capping layer of such structure would give rise to substantial mass loss from molecularly adsorbed MMA at low temperatures, with additional MMA and $CH_2{=}NH$ being produced at higher temperatures (above 350 °C) from decomposition/recombination of dissociatively adsorbed species, strongly bound to Al, giving rise to nitride-like Al and N XPS binding energies. The one surprise is that H_2 is observed to desorb primarily below 100 °C (Figure 9), i.e., far below the temperatures where dehydrogenation reactions of adsorbed CH_xNH_y species might be expected. We note that copious H_2 is produced during milling, and it is possible that some becomes physically trapped in the layer of MMA bound to the particles and, thus, desorbs along with the MMA.

■ ASSOCIATED CONTENT

Supporting Information

Additional XPS, TGA-MS, and computational results are presented, along with additional details regarding the computation strategy. This material is available free of charge via the Internet at http://pubs.acs.org/.The Supporting Information is available free of charge on the ACS Publications website at DOI: 10.1021/acsami.5b04806.

■ AUTHOR INFORMATION

Corresponding Author

*Tel: (+1) 801-585-7289, E-mail: anderson@chem.utah.edu.

Author Contributions

J.A.B. and S.L.A. are senior authors.

Notes

The authors declare no competing financial interest.

■ ACKNOWLEDGMENTS

The Utah authors acknowledge support from the Air Force Office of Scientific Research under AFOSR MURI Grant FA9550-08-1-0400 and BRI Grant FA9550-12-1-0481. We are grateful to Bo Hu and Tianpin Wu at the Advanced Photon Source (APS) for attempting FTIR spectroscopy. APS is an Office of Science User Facility operated for the U.S. Department of Energy (DOE) Office of Science by Argonne National Laboratory, and it was supported by the U.S. DOE under Contract No. DE-AC02-06CH11357. A grant of computer time from the Department of Defense High Performance Computing Modernization Program on the five DoD Supercomputing Resource Centers (Air Force Research Laboratory, Army Research Laboratory, Engineer Research and Development Center, Navy, and Maui High Performance Computing Center) is gratefully acknowledged. This work made use of University of Utah shared facilities of the Micron Technology Foundation Inc., the Microscopy Suite sponsored by the College of Engineering, Health Sciences Center, Office of the Vice President for Research, and the Utah Science Technology and Research (USTAR) initiative of the State of Utah.

■ REFERENCES

(1) Ivanov, G. V.; Tepper, F. In *"Activated" Aluminum as a Stored Energy Source for Propellants*; Begell House: pp 636–645.
(2) Mench, M. M.; Yeh, C. L.; Kuo, K. K., Propellant Burning Rate Enhancement and Thermal Behavior of Ultra-Fine Aluminum Powders (ALEX). *Int. Conf. ICT* **1998**, *29th*, 30.1–30.15.
(3) MacKenzie, S. *Handbook of Aluminum*; Marcel Decker, Inc.: New York, Basel, 2003; Vol. *1*, p 1309.
(4) Galfetti, L.; Luca, L. T. D.; Severini, F.; Meda, L.; Marra, G.; Marchetti, M.; Regi, M.; Bellucci, S. Nanoparticles for Solid Rocket Propulsion. *J. Phys.: Condens. Matter* **2006**, *18*, S1991–S2005.
(5) Armstrong, R. W.; Baschung, B.; Booth, D. W.; Samirant, M. Enhanced Propellant Combustion with Nanoparticles. *Nano Lett.* **2003**, *3*, 253–255.
(6) Lynch, P.; Fiore, G.; Krier, H.; Glumac, N. Gas-Phase Reaction in Nanoaluminum Combustion. *Combust. Sci. Technol.* **2010**, *182*, 842–857.
(7) Connell, T. L., Jr.; Risha, G. A.; Yetter, R. A.; Young, G.; Sundaram, D. S.; Yang, V. Combustion of Alane and Aluminum with Water for Hydrogen and Thermal Energy Generation. *Proc. Combust. Inst.* **2011**, *33*, 1957–1965.
(8) Allen, D.; Krier, H.; Glumac, N. Heat Transfer Effects in Nano-Aluminum Combustion at High Temperatures. *Combust. Flame* **2014**, *161*, 295–302.
(9) Risha, G. A.; Son, S. F.; Yetter, R. A.; Yang, V.; Tappan, B. C. Combustion of Nano-Aluminum and Liquid Water. *Proc. Combust. Inst.* **2007**, *31*, 2029–2036.
(10) Yetter, R. A.; Risha, G. A.; Son, S. F. Metal Particle Combustion and Nanotechnology. *Proc. Combust. Inst.* **2009**, *32*, 1819–1838.
(11) Sundaram, D. S.; Yang, V.; Huang, Y.; Risha, G. A.; Yetter, R. A. Effects of Particle Size and Pressure on Combustion of Nano-Aluminum Particles and Liquid Water. *Combust. Flame* **2013**, *160*, 2251–2259.
(12) Wang, H.; Jian, G.; Yan, S.; DeLisio, J. B.; Huang, C.; Zachariah, M. R. Electrospray Formation of Gelled Nano-Aluminum Microspheres with Superior Reactivity. *ACS Appl. Mater. Interfaces* **2013**, *5*, 6797–6801.
(13) Nabiyouni, G.; Fesharaki, M. J.; Mozafari, M.; Amighian, J. Characterization and Magnetic Properties of Nickel Ferrite Nanoparticles Prepared by Ball Milling Technique. *Chin. Phys. Lett.* **2010**, *27*, 126401.
(14) Li, S.; Yan, W.; Zhang, W.-x. Solvent-Free Production of Nanoscale Zero-Valent Iron with Precision Milling. *Green Chem.* **2009**, *11*, 1618–1626.
(15) Oleszak, D.; Shingu, P. H. Nanocrystalline Metals Prepared by Low Energy Ball Milling. *J. Appl. Phys.* **1996**, *79*, 2975–2980.
(16) Perez, J. P. L.; McMahon, B. W.; Schneider, S.; Boatz, J. A.; Hawkins, T. W.; McCrary, P. D.; Beasley, P. A.; Kelley, S. P.; Rogers, R. D.; Anderson, S. L. Exploring the Structure of Nitrogen-Rich Ionic Liquids and Their Binding to the Surface of Oxide-Free Boron Nanoparticles. *J. Phys. Chem. C* **2013**, *117*, 5693–5707.
(17) Sepelak, V.; Duvel, A.; Wilkening, M.; Becker, K.-D.; Heitjans, P. Mechanochemical Reactions and Syntheses of Oxides. *Chem. Soc. Rev.* **2013**, *42*, 7507–7520.
(18) Rehbinder, P. A. New Physico-Chemical Phenomena in the Deformation and Mechanical Treatment of Solids. *Nature* **1947**, *159*, 866–867.

DOI: 10.1021/acsami.5b04806
ACS Appl. Mater. Interfaces 2015, 7, 16101–16116

(19) Barnoush, A.; Vehoff, H. Hydrogen Embrittlement of Aluminum in Aqueous Environments Examined by in Situ Electrochemical Nanoindentation. *Scr. Mater.* **2008**, *58*, 747−750.
(20) Gutman, E. M. *Mechanochemistry of Materials*; Cambridge International Science Publishing: Cambridge, 1998; pp 1−215.
(21) Bowmaker, G. A. Solvent-Assisted Mechanochemistry. *Chem. Commun. (Cambridge, U. K.)* **2013**, *49*, 334−348.
(22) Friščić, T.; Jones, W. Recent Advances in Understanding the Mechanism of Cocrystal Formation Via Grinding. *Cryst. Growth Des.* **2009**, *9*, 1621−1637.
(23) Friscic, T.; Trask, A. V.; Jones, W.; Motherwell, W. D. S. Screening for Inclusion Compounds and Systematic Construction of Three-Component Solids by Liquid-Assisted Grinding. *Angew. Chem., Int. Ed.* **2006**, *45*, 7546−7550.
(24) Syugaev, A. V.; Maratkanova, A. N.; Shakov, A. A.; Nelyubov, A. V.; Lomayeva, S. F. Surface Modification of Iron Particles with Polystyrene and Surfactants under High-Energy Ball Milling. *Surf. Coat. Technol.* **2013**, *236*, 429−437.
(25) Wu, H.; Zhao, W.; Hu, H.; Chen, G. One-Step in Situ Ball Milling Synthesis of Polymer-Functionalized Graphene Nanocomposites. *J. Mater. Chem.* **2011**, *21*, 8626.
(26) McMahon, B. W.; Perez, J. P. L.; Yu, J.; Boatz, J. A.; Anderson, S. L. Synthesis of Nanoparticles from Malleable and Ductile Metals Using Powder-Free, Reactant-Assisted Mechanical Attrition. *ACS Appl. Mater. Interfaces* **2014**, *6*, 19579−19591.
(27) Gallardo, I.; Pinson, J.; Vila, N. Spontaneous Attachment of Amines to Carbon and Metallic Surfaces. *J. Phys. Chem. B* **2006**, *110*, 19521−10529.
(28) Kasai, P. H.; Himmel, H. J. Insertion of the Al Atom into the NH_3 Molecule: Semiempirical SCF MO and Matrix Isolation ESR Study. *J. Phys. Chem. A* **2002**, *106*, 6765−6774.
(29) Joly, H. A.; Ashley, J.; Levesque, M. Y.; Rank, J. P. Electron Paramagnetic Resonance Study of the Mononuclear Al Species Formed in the Reaction of Al Atoms and Cyclopropylamine at 77 K in an Adamantane Matrix. *J. Phys. Chem. A* **2006**, *110*, 3911−3919.
(30) Joly, H. A.; Newton, T.; Myre, M. Activation of C-Cl by Ground-State Aluminum Atoms: An EPR and DFT Investigation. *Phys. Chem. Chem. Phys.* **2012**, *14*, 367−374.
(31) Jones, D. E. G.; Turcotte, R.; Fouchard, R. C.; Kwok, Q. S. M.; Turcotte, A.-M.; Abdel-Qader, Z. Hazard Characterization of Aluminum Nanopowder Compositions. *Propellants, Explos., Pyrotech.* **2003**, *28*, 120−131.
(32) Polunina, I. A.; Roldugin, V. I.; Kolesnikova, T. P.; Buryak, A. K.; Ulyanov, A. V.; Polunin, K. E. Interaction between Carboxylic Modifiers and Nanodispersed Aluminium. *Colloids Surf., A* **2004**, *239*, 85−93.
(33) Davies, P. R.; Newton, N. G. The Chemisorption and Decomposition of Pyridine and Ammonia at Clean and Oxidised Al(111) Surfaces. *Surf. Sci.* **2003**, *546*, 149−158.
(34) Perez, J. P. L.; Yu, J.; Sheppard, A. J.; Chambreau, S. D.; Vaghjiani, G. L.; Anderson, S. L. Binding of Alkenes and Ionic Liquids to B-H Functionalized Boron Nanoparticles: Creation of Particles with Controlled Dispersibility and Minimal Surface Oxidation. *ACS Appl. Mater. Interfaces* **2015**, *7*, 9991−10003.
(35) Zhao, Y.; Truhlar, D. G. The M06 Suite of Density Functionals for Main Group Thermochemistry, Thermochemical Kinetics, Noncovalent Interactions, Excited States, and Transition Elements: Two New Functionals and Systematic Testing of Four M06-Class Functionals and 12 Other Functionals. *Theor. Chem. Acc.* **2008**, *120*, 215−241.
(36) McLean, A. D.; Chandler, G. S. Contracted Gaussian Basis Sets for Molecular Calculations. I. Second Row Atoms, Z=11−18. *J. Chem. Phys.* **1980**, *72*, 5639−5648.
(37) Francl, M. M.; Pietro, W. J.; Hehre, W. J.; Binkley, J. S.; Gordon, M. S.; DeFrees, D. J.; Pople, J. A. Self-Consistent Molecular Orbital Methods. XXIII. A Polarization-Type Basis Set for Second-Row Elements. *J. Chem. Phys.* **1982**, *77*, 3654−3665.
(38) Clark, T.; Chandrasekhar, J.; Spitznagel, G. W.; Schleyer, P. v. R. Efficient Diffuse Function-Augmented Basis Sets for Anion Calculations. III. The 3-21+G Basis Set for First-Row Elements, Li-F. *J. Comput. Chem.* **1983**, *4*, 294−301.
(39) Krishnan, R.; Binkley, J. S.; Seeger, R.; Pople, J. A. Self-Consistent Molecular Orbital Methods. XX. A Basis Set for Correlated Wave Functions. *J. Chem. Phys.* **1980**, *72*, 650−654.
(40) Perez, J. P. L.; McMahon, B. W.; Yu, J.; Schneider, S.; Boatz, J. A.; Hawkins, T. W.; McCrary, P. D.; Flores, L. A.; Rogers, R. D.; Anderson, S. L. Boron Nanoparticles with High Hydrogen Loading: Mechanism for B−H Binding and Potential for Improved Combustibility and Specific Impulse. *ACS Appl. Mater. Interfaces* **2014**, *6*, 8513−8525.
(41) Gonzalez, C.; Schlegel, H. B. An Improved Algorithm for Reaction Path Following. *J. Chem. Phys.* **1989**, *90*, 2154−2161.
(42) Schmidt, M. W.; Baldridge, K. K.; Boatz, J. A.; Elbert, S. T.; Gordon, M. S.; Jensen, J. H.; Koseki, S.; Matsunaga, N.; Nguyen, K. A.; Su, S.; Windus, T. L.; Dupuis, M.; Montgomery, J. A General Atomic and Molecular Electronic Structure System. *J. Comput. Chem.* **1993**, *14*, 1347−1363.
(43) Gordon, M. S.; Schmidt, M. W. *Advances in Electronic Structure Theory, in Theory and Applications of Computational Chemistry: The First Forty Years*; Dykstra, C., Frenking, G., Kim, K., Scuseria, G., Eds.; Elsevier: Amsterdam, 2005; pp 1167−1190.
(44) Bockmon, B. S.; Pantoya, M. L.; Son, S. F.; Asay, B. W.; Mang, J. T. Combustion Velocities and Propagation Mechanisms of Metastable Interstitial Composites. *J. Appl. Phys.* **2005**, *98*, 064903.
(45) Henderson, M. A. An HREELS and TPD Study of Water on TiO_2(110): The Extent of Molecular Versus Dissociative Adsorption Surf. *Surf. Sci.* **1996**, *355*, 151−166.
(46) Moulder, J. F.; Stickle, W. F.; Sobol, P. E.; Bomben, K. D. Handbook of X-Ray Photoelectron Spectroscopy; Perkin-Elmer Corporation: Eden Prairie, 1992; p 261.
(47) Powell, C. J.; Jablonski, A. NIST Electron Effective Attenuation Length Database Version 1.3, Srd 82. National Institute of Standards and Technology: Gaithersburg, MD, 2011.
(48) Balchev, I.; Minkovski, N.; Marinova, T.; Shipochka, M.; Sabotinov, N. Composition and Structure Characterization of Aluminum after Laser Ablation. *Mater. Sci. Eng., B* **2006**, *135*, 108−112.
(49) Chenakin, S. P.; Prada Silvy, R.; Kruse, N. Effect of X-Rays on the Surface Chemical State of Al_2O_3, V_2O_5, and Aluminovanadate Oxide. *J. Phys. Chem. B* **2005**, *109*, 14611−14618.
(50) Kloprogge, J. T.; Duong, L. V.; Wood, B. J.; Frost, R. L. XPS Study of the Major Minerals in Bauxite: Gibbsite, Bayerite and (Pseudo-)Boehmite. *J. Colloid Interface Sci.* **2006**, *296*, 572−576.
(51) Kwon, Y.-S.; Gromov, A. A.; Ilyin, A. P.; Rim, G.-H. Passivation Process for Superfine Aluminum Powders Obtained by Electrical Explosion of Wires. *Appl. Surf. Sci.* **2003**, *211*, 57−67.
(52) Laidani, N.; Vanzetti, L.; Anderle, M.; Basillais, A.; Boulmer-Leborgne, C.; Perriere, J. Chemical Structure of Films Grown by Aln Laser Ablation: An X-Ray Photoelectron Spectroscopy Study. *Surf. Coat. Technol.* **1999**, *122*, 242−246.
(53) Lewis, W. K.; Rosenberger, A. T.; Gord, J. R.; Crouse, C. A.; Harruff, B. A.; Fernando, K. A. S.; Smith, M. J.; Phelps, D. K.; Spowart, J. E.; Guliants, E. A.; Bunker, C. E. Multispectroscopic (FTIR, XPS, and TOFMS-TPD) Investigation of the Core-Shell Bonding in Sonochemically Prepared Aluminum Nanoparticles Capped with Oleic Acid. *J. Phys. Chem. C* **2010**, *114*, 6377−6380.
(54) Schoser, S.; Bräuchle, G.; Forget, J.; Kohlhof, K.; Weber, T.; Voigt, J.; Rauschenbach, B. XPS Investigation of Aln Formation in Aluminum Alloys Using Plasma Source Ion Implantation. *Surf. Coat. Technol.* **1998**, *103−104*, 222−226.
(55) Zähr, J.; Oswald, S.; Türpe, M.; Ullrich, H. J.; Füssel, U. Characterisation of Oxide and Hydroxide Layers on Technical Aluminum Materials Using XPS. *Vacuum* **2012**, *86*, 1216−1219.
(56) Mullins, W. M.; Averbach, B. L. The Electronic Structure of Anodized and Etched Aluminum Alloy Surfaces. *Surf. Sci.* **1988**, *206*, 52−60.
(57) Taylor, J. A.; Rabalais, J. W. Reaction of Nitrogen (N_2^+) Beams with Aluminum Surfaces. *J. Chem. Phys.* **1981**, *75*, 1735−45.

DOI: 10.1021/acsami.5b04806
ACS Appl. Mater. Interfaces 2015, 7, 16101−16116

(58) Baker, C. C.; Ceylan, A.; Shah, S. I. Reactive Gas Condensation Synthesis of Aluminum Nitride Nanoparticles. *J. Nanosci. Nanotechnol.* **2006**, *6*, 146−150.
(59) Affrossman, S.; MacDonald, S. M. Adsorption Modes of a Model Adhesive Resin, (Methylamino)Ethanol, on Aluminum and Phosphated Aluminum Surfaces. *Langmuir* **1996**, *12*, 2090−2095.
(60) Alexander, M. R.; Thompson, G. E.; Beamson, G. Characterization of the Oxide/Hydroxide Surface of Aluminium Using X-Ray Photoelectron Spectroscopy: A Procedure for Curve Fitting the O 1s Core Level. *Surf. Interface Anal.* **2000**, *29*, 468−477.
(61) Rangan, S.; Bournel, F.; Gallet, J. J.; Kubsky, S.; Le Guen, K.; Dufour, G.; Rochet, F.; Sirotti, F.; Carniato, S.; Ilakovac, V. Experimental and Theoretical NEXAFS/XPS Study of the Room-Temperature Adsorption of Acetonitrile on Si(001)-2 × 1. *Phys. Rev. B: Condens. Matter Mater. Phys.* **2005**, *71*, 165319/1−165319/11.
(62) Adenier, A.; Chehimi, M. M.; Gallardo, I.; Pinson, J.; Vila, N. Electrochemical Oxidation of Aliphatic Amines and Their Attachment to Carbon and Metal Surfaces. *Langmuir* **2004**, *20*, 8243−8253.
(63) Baláž, P.; Achimovičová, M.; Baláž, M.; Billik, P.; Cherkezova-Zheleva, Z.; Criado, J. M.; Delogu, F.; Dutková, E.; Gaffet, E.; Gotor, F. J.; Kumar, R.; Mitov, I.; Rojac, T.; Senna, M.; Streletskiik, A.; Wieczorek-Ciurowa, K. Hallmarks of Mechanochemistry: From Nanoparticles to Technology. *Chem. Soc. Rev.* **2013**, *42*, 7571−7637.
(64) Trefry, J. C.; Monahan, J. L.; Weaver, K. M.; Meyerhoefer, A. J.; Markopolous, M. M.; Arnold, Z. S.; Wooley, D. P.; Pavel, I. E. Size Selection and Concentration of Silver Nanoparticles by Tangential Flow Ultrafiltration for Sers-Based Biosensors. *J. Am. Chem. Soc.* **2010**, *132*, 10970−10972.
(65) Stein, S. E., director. IR and Mass Spectra. In NIST Chemistry Webbook, NIST Standard Reference Database Number 69; Mallard, W. G., Linstrom, P. J., Eds.; NIST Mass Spec Data Center, National Institute of Standards and Technology: Gaithersburg, MD 20899, (http://webbook.nist.gov). 2000.
(66) Cao, X.; Hamers, R. J. Molecular and Dissociative Bonding of Amines with the Si(111)-(7 × 7) Surface. *Surf. Sci.* **2003**, *523*, 241−251.
(67) Hansen, U.; Vogl, P.; Fiorentini, V. Quasiharmonic Versus Exact Surface Free Energies of Al: A Systematic Study Employing a Classical Interatomic Potential. *Phys. Rev. B: Condens. Matter Mater. Phys.* **1999**, *60*, 5055−5064.
(68) Vitos, L.; Ruban, A. V.; Skriver, H. L.; Kollar, J. The Surface Energy of Metals. *Surf. Sci.* **1998**, *411*, 186−202.
(69) Kumikov, V. K.; Khokonov, K. B. On the Measurement of Surface Free Energy and Surface Tension of Solid Metals. *J. Appl. Phys.* **1983**, *54*, 1346−50.
(70) Wang, X.; Jia, Y.; Yao, Q.; Wang, F.; Ma, J.; Hu, X. The Calculation of the Surface Energy of High-Index Surfaces in Metals at Zero Temperature. *Surf. Sci.* **2004**, *551*, 179−188.
(71) Kammeyer, C. W.; Whitman, D. R. Quantum Mechanical Calculation of Molecular Radii. I. Hydrides of Elements of Periodic Groups IV through VII. *J. Chem. Phys.* **1972**, *56*, 4419−4421.
(72) Watson, P. R.; Hove, M. A. V.; Hermann, K. Atlas of Surface Structures. *J. Phys. Chem. Ref. Data* **1994**, *Monograph 5*, 1−907.

DOI: 10.1021/acsami.5b04806
ACS Appl. Mater. Interfaces 2015, 7, 16101−16116